Mind the gap : gas and dust in planet-forming disks

Marel, N.

9

The (w)hole survey: transition disk candidates from the Spitzer catalogs

van der Marel, N.; Verhaar, B.W.; Terwisga, S., Merín, B.; Herczeg, G.J.; Ligterink, N.F.W.; van Dishoeck, E.F. *The (w)hole survey: an unbiased sample study of transition disk candidates from the Spitzer catalogs.* in prep.

Abstract

Understanding disk evolution and dissipation is essential for studies of planet formation. Transition disks, i.e., disks with large dust cavities, are promising candidates of active evolution. About two dozen SED-selected candidates have been confirmed to have dust cavities through millimeter interferometric imaging, but this sample is biased towards the brightest disks. We aim to find a large unbiased sample of transition disk candidates in nearby star-forming regions for studying their global properties as well as their origin. The *Spitzer* surveys of nearby low-mass star forming regions have resulted in more than 4000 Young Stellar Objects (YSOs). Using color criteria we have selected a sample of ~150 candidates, and an additional 40 candidates and known transition disks from the literature. The *Spitzer* data were complemented by new observations at longer wavelengths, including new JCMT and APEX submillimeter photometry, and *WISE* and *Herschel*-PACS mid and far-infrared photometry. Furthermore, optical and near infrared spectroscopy was obtained and stellar types were derived for 85% of the sample, including the information from the literature. The SEDs were fit to a grid of RADMC-3D disk models with a limited number of parameters: disk mass, inner disk mass, scale height and flaring, and disk cavity radius, where the latter is the main parameter of interest. A large fraction of the targets turn out to have dust cavities based on the SED. The derived cavity sizes are consistent with imaging/modeling results in the literature, where available. Trends are found with $L_{\rm disk}/L_*$ and stellar mass and a possible connection with exoplanet orbital radii. A comparison with a previous study where color observables are used (Cieza et al. 2010) reveals large overlap between their category of planet-forming disks and our transition disks with cavities. The color criteria are a proper tool to select transition disk candidates. In this work we present a large number of transition disks that are suitable for follow-up observations with ALMA.

9.1 Introduction

A central question in planet formation is how the optically thick protoplanetary disks around classical T Tauri stars evolve into the optically thin debris disks around older systems (Williams & Cieza 2011). An important part of the evolution occurs in the transitional phase between these two regimes. Transitional disks, disks with inner dust cavities, are considered to form the evolutionary link, although it remains uncertain whether all disks go through this phase at some point during their lifetime (e.g. Cieza et al. 2007; Currie & Kenyon 2009). The transition disk fraction is thought to be 5%-25% depending on the definition, implying that the evolutionary path through a transition disk is either rapid or uncommon. Transitional disk candidates are traditionally identified through a deficit of infrared flux in the mid-IR spectral energy distribution (SED) (e.g. Strom et al. 1989; Calvet et al. 2002; Espaillat et al. 2014, for review). The deficit arises from the absence of hot small dust particles close to the star, which can be caused by either grain growth, photoevaporative clearing or interaction with a stellar companion or recently formed planet, all processes closely linked to disk evolution. Thanks to *Spitzer* mid-infrared spectroscopy surveys, a large number of transitional disks has been discovered through the dip in their SED (e.g. Brown et al. 2007; Najita et al. 2007; Kim et al. 2009; Merín et al. 2010). Submillimeter observations of about two dozen of the brightest disks have directly resolved large holes with pioneering interferometers, confirming their transition disk status (e.g. Piétu et al. 2005; Brown et al. 2008, 2009; Isella et al. 2010a,b; Andrews et al. 2011). The hole sizes generally match well with estimates from SED modeling, suggesting that the current interpretation and modeling of SEDs can correctly infer this parameter provided that the mid-infrared part of the SED is well covered observationally. The Atacama Large Millimeter/submillimeter Array (ALMA) has produced even sharper dust images of a small sample of transition disks with evidence for dust trapping (van der Marel et al. 2013; Casassus et al. 2013; Pérez et al. 2014; Zhang et al. 2014). ALMA has also revealed the gas distribution through CO observations, showing that substantial amounts of gas are present inside the dust cavities (Bruderer et al. 2014; van der Marel et al. 2015c; Perez et al. 2015; van der Marel et al. 2015b). However, ALMA has so far focused on the most well-studied and brightest transition disks. For a better understanding of the role of transition disks in the disk evolution and planet formation process, a large unbiased sample of transition disks with large holes is required to study the general picture.

One of the most exciting explanations for transition disks is the presence of a young planet that has cleared out its orbit (Lin & Papaloizou 1979). This scenario has been confirmed through the tentative detection of planets embedded in transition disks through direct imaging for a handful of disks (Huélamo et al. 2011; Kraus & Ireland 2012; Quanz et al. 2013; Reggiani et al. 2014; Quanz 2015). As it remains unclear how and at what stage planets are formed in a disk, finding them at the earliest stage and study of their environment can provide important clues on the planet formation process.

Transition disk candidates have been identified through a range of different criteria (Brown et al. 2007; Muzerolle et al. 2010; Oliveira et al. 2010; Merín et al. 2010; Cieza et al. 2010, 2012b; Romero et al. 2012), usually involving the Spitzer colors in the (mid) infrared. The availability of *Spitzer* IRS spectra between 5-35 μm was crucial for classification and determination of the hole size in these studies especially in covering the 8-20 micron region where the SEDs reach their minimum but which is not well covered by the 8 and 24 micron photometry points. In recent years, far infrared *Herschel* PACS and SPIRE photometry has been used to identify and characterize (transition) disks (e.g Ribas et al. 2013; Bustamante et al. 2015; Rebollido et al. 2015). Other studies identified candidates by comparing the infrared part of their SEDs with the 'median' T Tauri disk SED (e.g. Harvey et al. 2007; Merín et al. 2008).

These studies define a separate class of transition disks as 'anemic' disks: disks with homologous depletion of dust due to grain growth or settling at all radii, exhibiting a low infrared excess at all wavelengths. Furthermore, some studies distinguish between pre-transitional and transitional disks: disks with a gap (inner disk present inside the cavity) and disks with a hole (Espaillat et al. 2007) although there is no obvious evolutionary connection. A 'cold disk' (Brown et al. 2007) refers to a transition disk with a strong deficit in the mid infrared, implying a cavity with a steep inner wall. Note that a few transition disks have been found in millimeter imaging without evidence for mid infrared dip in their SED, e.g. MWC 758 (Isella et al. 2010b)

Selection of candidates is sometimes followed up by radiative transfer modeling of the radial disk structure, to constrain the dust cavity size and disk mass (Kim et al. 2009; Merín et al. 2010) to determine the origin of the cavity besides clearing by a companion. Increased grain growth in the inner part of disk would result in the appearance of a dust deficit in the SED (Dullemond & Dominik 2005), although this would not be visible in millimeter imaging (Birnstiel et al. 2010). Furthermore, multiplicity studies can define the origin of the cavity as circumbinary disk whereas measuring the accretion through optical Hα can determine photoevaporative clearing (Najita et al. 2007; Espaillat et al. 2007; Cieza et al. 2010). Theoretical work has also shown that photoevaporative clearing cannot explain the largest observed cavities and a combination of processes may be responsible (Owen & Clarke 2012; Rosotti et al. 2013).

Overall, the definition of a transition disk candidate remains loose and has been used in various contexts in different studies. Due to lack of a large sample of transition disks, general properties remain uncertain and it is still unclear whether the origin for all transition disk cavities is the same, or whether disks follow different evolutionary paths (Cieza et al. 2007). Also, the distribution of cavity radii is not known, while this could constrain the birth sites of giant planets before migration. The analysis of a large unbiased sample of transition disks and candidates will provide firm constraints on their general properties. *Spitzer* surveys in all nearby (<500 pc) star-forming regions (Cores to Disks (c2d), Gould-Belt (GB) and Taurus) have provided identification and SEDs of several thousands of Young Stellar Objects (YSOs) (e.g. Evans et al. 2009; Rebull et al. 2010; Dunham et al. 2015, and references therein), out of which many transition disk candidates. In addition, in recent years the AllWISE catalog with mid infrared targets has become available (Wright et al. 2010), and the *Herschel* telescope (Pilbratt et al. 2010) has observed large parts of nearby star forming regions in the far infrared. Due to the availability of *Spitzer* data combined with WISE and *Herschel* data, the timing is perfect for a large transition disk SED survey.

In this work, we analyze transition disk candidates selected from the *Spitzer* catalogs using robust color criteria developed by Merín et al. (2010). These criteria were developed after deep analysis of the SEDs including IRS spectra. Our sample is complemented by additional candidates and known transition disks from the literature. The SEDs are complemented with optical, new archival far infrared *Herschel*, *Spitzer* IRS spectra (where available) and new submillimeter observations and modeled using the dust radiative transfer code RADMC-3D with a generic disk structure with a cavity. The main parameter of interest is the cavity size $r_{\rm cav}$. In Section 9.2 we discuss the selection criteria of the sample and the additional observations, Section 9.3 presents the results of the observations, Section 9.4 discusses the modeling procedure and limitations and the resulting disk parameters and in Section 9.5 we discuss the robustness of the sample and comparison with previous studies. One of the aims of this study is to define an unbiased sample of transition disks with dust cavities that are large enough to be imaged in the future by ALMA ($\geq$10 AU or $\sim$0.03", for the largest distances). The resolved images of gas and dust will provide more clues on the origin of the dust cavities and the place

of transition disks in disk evolution.

9.2 Observations

9.2.1 Target selection

The c2d, GB and Taurus *Spitzer* Legacy programs completed full infrared surveys using the Infrared Array Camera (IRAC; 3.6-8.0 μm) and Multiband Imaging Photometer (MIPS; 24-160 μm) in the nearby star-forming regions ($\leq$450 pc), resulting in more than 4000 identified YSOs (see Table 9.1 for an overview of papers presenting the data). Several bright YSOs from the c2d survey were targeted for additional observation with the *Spitzer* InfraRed Spectrograph (IRS; 5-35 μm). Merín et al. (2010, hereafter M10) analyzed 35 possible transition disk candidates for which IRS spectra were available in detail through SED modeling, and defined two sets of color criteria:

$$\begin{aligned} [\mathrm{A}] : 0.0 < [3.6] - [8.0] < 1.1; \\ 3.2 < [8.0] - [24.0] < 5.3; \end{aligned} \tag{9.1}$$

$$\begin{aligned} [\mathrm{B}] : 1.1 < [3.6] - [8.0] < 1.8; \\ 3.2 < [8.0] - [24.0] < 5.3; \end{aligned} \tag{9.2}$$

where the bracketed numbers refer to the magnitudes at the *Spitzer* wavelengths. The Region A criteria select 'clean' inner holes (disks for which there is no substantial excess in any IRAC band and there is a clear signature of an inner dust hole) and the Region B criteria select disks with a clear signature of an inner dust hole, but some excess in the IRAC bands, possibly resulting from an inner disk. The latter criterion includes several of the confirmed imaged transition disks (Brown et al. 2009; Andrews et al. 2009), but may also include some disks without holes (M10).

M10 finds one transition disk with a particularly large hole (Sz 84, object 17), which falls outside of the color criteria mentioned above. Inspection of its SED reveals a steep slope between the 24 μm and 70 μm flux. Therefore we set an additional color criterium:

$$\begin{aligned} [\mathrm{L}] : 0.0 < [3.6] - [8.0] < 1.1; \\ 10.0 > [24.0] - [70.0] > 3.8; \end{aligned} \tag{9.3}$$

In this case the MIPS-2 flux at 70 μm has to be detected rather than an upper limit. Due to the large beam size of *Spitzer* at 70 μm (18", see Table 9.3), this flux can be confused with nearby sources. The long wavelength flux thus has to be taken with extra care for the Region L criteria. The Region L targets are not mutually exclusive with the Region A criteria: some targets follow in both.

The color criteria were applied to the three main *Spitzer* catalogs, resulting in 153 candidates. In addition to the catalogs, we searched the literature for additional transition disk candidates, by using the color criteria on *Spitzer* targets that were not included in the catalogs (row 'Other' in Table 9.2), finding an additional 12 disks. Targets in Orion, Cepheus (Kirk et al. 2009) and IC 5146 (Harvey et al. 2008) are not included due to their large distances (450, 500 and 950 pc respectively). Finally, we added 7 confirmed transition disks known from resolved millimeter imaging and 21 targets that were marked as transition disk candidate by various authors, but were not yet included by the color criteria. The number of targets from various selections are listed in Table 9.2 with corresponding references. All targets in

the sample are listed in Table 9.12. Several of the color-selected targets have been identified as transition disk candidates or confirmed by millimeter imaging, as indicated in the last column of Table 9.12.

The distance to Serpens has been uncertain for a long time, with values between 250 and 400 pc (discussion in e.g. Oliveira et al. 2009). However, VLBA observations have demonstrated a distance of 415 pc for the Main Cloud (Dzib et al. 2010), which has been used in more recent work (Erickson et al. 2015; Ortiz-León et al. 2015), and has also been used in this study.

Table 9.1: *Overview Spitzer papers of YSOs in star forming regions*

Cores to Disks (c2d)		d (pc)	Paper
Ophiuchus (MIPS)	Padgett et al. (2008)	120	VII
Serpens	Harvey et al. (2007)	250-400[a]	IX
Cham II	Alcalá et al. (2008)	180	X
Lupus I,III,IV	Merín et al. (2008)	150-200	XI
Perseus	Young et al. (2015)	250	XII
WTTS (c2d)	Padgett et al. (2006); Cieza et al. (2007)	-	
Disks with holes (c2d)	Merín et al. (2010)	-	
	Gould Belt (GB)		
IC5146	Harvey et al. (2008)	950	I
Cepheus	Kirk et al. (2009)	300	II
CrA	Peterson et al. (2011)	150	III
Lupus V & VI (full)	Spezzi et al. (2011)	150	IV
Ophiuchus North	Hatchell et al. (2012)	120	V
Auriga	Broekhoven-Fiene et al. (2014)	450	VI
	Others		
η Cham (IRAC)	Megeath et al. (2005)	97	
η Cham (MIPS)	Sicilia-Aguilar et al. (2009)	97	
Cham I	Luhman et al. (2008)	160	
Taurus	Rebull et al. (2010); Luhman et al. (2010)	140	
λ Orionis	Hernández et al. (2010)	450	
Orion	Megeath et al. (2012)	450	
	Wahhaj et al. (2010)		
FEPS	Carpenter et al. (2008)	-	

Notes. [(a)] The distance to Serpens has been uncertain for a long time, but with recent VLBA observations it has been set to 415 pc (Dzib et al. 2011), which has been used in this study.

9.2.2 Additional photometry

For each target, an SED was constructed using the *Spitzer* IRAC and MIPS photometry, complemented with optical B, V and R data from the NOMAD catalog (Zacharias et al. 2005) and near infrared J, H and K photometry from 2MASS (Cutri et al. 2003). Reduced *Spitzer* IRS low-res spectra of 5-35 μm were taken from the Cornell Atlas of Spitzer/IRS Sources (CASSIS) (Lebouteiller et al. 2011) when available. For ID63 (DoAr28), the IRS spectrum in CASSIS included extended emission, a properly reduced spectrum was kindly provided by Melissa McClure (McClure et al. 2010). Unfortunately IRS spectra are not available for the entire sample, while colors only provide limited constraints on the derived cavity size. Bright isolated targets could be complemented with *IRAS* photometry, especially when *Spitzer* data

Table 9.2: *Target selection in each catalog*

Catalog/Criterion	[A]	[B]	[L]
c2d (Evans et al. 2009)	30	34	9
GB (Dunham et al. 2015)	25	15	31
Taurus (Rebull et al. 2010)	7	12	6
Other samples[a]	7	4	1
Additional targets[b]	7 imaging 21 SED		

Notes. [(a)] Targets were selected using our color criteria in the following papers, for targets not included in the c2d/GB/Taurus catalogs: Padgett et al. (2006); Silverstone et al. (2006); Carpenter et al. (2008); Luhman et al. (2008); Kim et al. (2009); Sicilia-Aguilar et al. (2009); Cieza et al. (2010); Luhman et al. (2010) [(b)] Some targets were added from the literature that did not follow the color criteria. Imaging targets were taken from Piétu et al. (2006); Ohashi (2008); Brown et al. (2009); Isella et al. (2010a); Andrews et al. (2010, 2011); Rosenfeld et al. (2013); van der Marel et al. (2013). The other targets were identified as transition disk candidate by Megeath et al. (2005); Hernández et al. (2007); Merín et al. (2008); Monnier et al. (2008); Hughes et al. (2008); Sicilia-Aguilar et al. (2008); Ireland & Kraus (2008); Kim et al. (2009); McClure et al. (2010); Najita et al. (2010); Espaillat et al. (2011); Furlan et al. (2011)

were saturated. The *Wide-field Infrared Survey Explorer (WISE)* performed an all sky survey in four wavelength bands: 3.4, 4.6, 12.0 and 22 μm leading to the AllWISE Source catalog (Wright et al. 2010). The coordinates of the targets in our sample were matched with the WISE targets (within 2") and the fluxes were added to the SEDs. Although 3 of the 4 bands overlap with *Spitzer*, the 12 μm flux provides an important data point in between IRAC and MIPS wavelengths when no IRS spectra are available. Furthermore, the diffraction limited beam size of the *WISE* satellite is twice as large as the *Spitzer* beam (see Table 9.3). The comparison between the *WISE* 22 μm flux with the MIPS-1 24 μm flux gives an independent check of confusion at longer wavelengths: if the 22 μm flux is much larger, there is likely a nearby source that will confuse 70 μm MIPS-2 flux as well. Although the *Spitzer* c2d and GB catalogs provide a quality flag on the MIPS-2 flux (MP2_Q_det_c) for possible confusion, this independent alternative check showed more directly which targets were confused at longer wavelengths. A difference between the 22 and 24 μm flux could also originate from infrared variability, for example due to a scale height changes in the inner disk (e.g. Flaherty & Muzerolle 2010; Espaillat et al. 2011). However, such variability is typically on the order of 20-40%. Therefore, we only consider confusion if the difference in flux is more than 50%. The fluxes of different telescopes are taken with years in between, so without infrared monitoring there is no possibility to quantify this effect for the targets in our sample, but the effect on our SED modeling is expected to be minor. The following targets were removed from the sample due to possible confusion and their SEDs were not further analyzed: IDs 30, 32, 82, 85, 86, 88, 90, 92, 93, 95, 97, 98, 116, 123, 126, 202, 346 and 347.

At longer wavelengths, the SEDs were complemented with (sub)millimeter data from the literature where available (see refs in Table 9.14). A subsample of the remaining targets were observed with the James Clerk Maxwell Telescope (JCMT) [1] and the Atacama Pathfinder

[1]The James Clerk Maxwell Telescope has historically been operated by the Joint Astronomy Centre on behalf of the Science and Technology Facilities Council of the United Kingdom, the National Research Council of Canada and the Netherlands Organisation for Scientific Research. Additional funds for the construction of SCUBA-2 were provided by the Canada Foundation for Innovation.

Table 9.3: *Beam sizes and apertures for photometry*

Telescope	Instrument	Wavelength range (μm)	Beam size/ Aperture(")
Spitzer	IRAC	3.6,4.5,5.8,8.0	1.7–1.9
	MIPS	24.0,70.0	6.0,18
WISE		3.4,4.6,12,22	6.1,6.4,6.5,12
Herschel	PACS	70,100,160	5.5,6.5,11
APEX	SABOCA	350	7.8
	LABOCA	870	19
JCMT	SCUBA-2	850	15

Experiment (APEX) [2]. Targets were selected on their expected submillimeter brightness considering their 70 μm flux. The details of these observations are discussed in Section 9.2.3.

The SEDs were further complemented with far infrared fluxes from the *Herschel* Space Observatory (Pilbratt et al. 2010). The data reduction is discussed in Section 9.2.4.

9.2.3 Submillimeter observations

Observations of 32 of our targets were taken with the SABOCA and/or LABOCA instruments at the APEX telescope at the Chajnantor plateau in Chile. Observations were taken in service mode in 2012 and 2013 in ESO programs 089.C-0940, 090.C-0820 and 091.C-0822 and Max Planck programs M0010_88 and M0003_90. SABOCA is a 39-channel bolometer array operating at 350 μm (Siringo et al. 2010), LABOCA is a 295-channel bolometer array at 870 μm (Siringo et al. 2009). Imaging was performed in wobbler on-off mode. For a few sources, imaging was also performed in mapping mode (map size 1.5') to check the pointing and to check for extended emission. One source (MP Mus, ID 20) was observed with the new ArTeMiS camera in mapping during its commissioning phase, operating at 350 μm (Revéret et al. 2014). Integration times were 5-40 minutes on source. The data were reduced using the CRUSH software (Kovács 2008) and (for the wobbler observations) verified using the BoA software (Schuller 2012). The results from both reduction techniques were found to agree within error bars and the CRUSH results are reported in Table 9.8. Flux calibration uncertainties (not included in Table 9.8) are typically 10% for LABOCA and 25-30% for SABOCA.

Observations of 41 of our targets were taken with the SCUBA-2 instrument at the JCMT telescope at Mauna Kea, Hawaii. Observations were taken in service mode in 2012 and 2013 in programs M12AN07, M12BN13 and M13AN01. SCUBA-2 is a 10,000 pixel bolometer camera operating simultaneously at 450 and 850 μm (Holland et al. 2013). Imaging was performed in the smallest possible map size (Daisy 3' pattern). Observations were taken in grade 3-5 weather, which is generally insufficient for observing at 450 μm, so only the 850 μm data are considered. Integration times were 5-50 minutes on source. The data were reduced using the default online pipeline. The resulting FITS images were inspected by eye for extended emission and fluxes and noise levels were derived. The noise levels were estimated by measuring the standard deviation in the map, after subtraction of point sources. The results are reported in Table 9.7. The flux calibration uncertainty (not included in Table 9.7) is typically 10% for SCUBA-2.

[2]This publication is based on data acquired with the Atacama Pathfinder Experiment (APEX). APEX is a collaboration between the Max-Planck-Institut fur Radioastronomie, the European Southern Observatory, and the Onsala Space Observatory.

9.2.4 Herschel observations

We have searched the *Herschel* Science Archive for observations with the PACS broadband photometer (Poglitsch et al. 2010) at the coordinates of all targets in the sample. In photometry mode, PACS observes simultaneously at either 70 (PACS blue) and 160 μm (PACS red) or 100 (PACS green) and 160 μm. Therefore, targets are recovered in either two or three of these wavelength bands. Only data products of reduction level higher than 2.0 were used, using the high pass filter.

Photometry of the PACS data was performed using the *annularSkyAperturePhotometry*-task in the Herschel Interactive Processing Environment (HIPE), version 12.1.0. This task derives background-corrected fluxes from point sources by comparing the flux inside a region centered on the point source and an annulus around it. We used the values for the aperture and annulus radii as used by Ribas et al. (2013). The background was estimated using the DAOPhot algorithm. Errors were estimated manually at several positions near the source position, to avoid including nearby extended emission originating from clouds. The presence of nearby clouds is indicated in Table 9.13. The flux calibration uncertainty (not included in Table 9.13) is typically 5% for PACS photometry.

9.2.5 Spectroscopy

Stellar properties such as the spectral type must be determined to correct for the extinction and deredden the SED flux points. The stellar luminosity is required to understand and interpret the SEDs properly. For about half of the targets in the sample, spectral types are available from the literature. The targets without known spectral type were observed with optical or near-infrared spectroscopy (the latter for targets that are optically faint due to high extinction).

Optical

Optical spectra were taken for 90 targets, including reobservation of 24 targets for which the literature spectral type was still uncertain (see Table 9.4). These observations were taken during 5 nights in visitor mode in August 2012 at the 4.2m William Herschel Telescope (WHT) at La Palma, using the Intermediate dispersion Spectrograph and Imaging System (ISIS) spectrograph. We used the double arm to obtain spectra between 3200–10000 Å with resolving power of $\sim$ 1000, using the R316R and R600B gratings. R magnitudes ranged between 9 and 19 mags, requiring integration times between 1 and 60 minutes. The slit width was set each night depending on the seeing.

The images were reduced and spectra extracted using standard methods with custom codes in IDL. All spectra were flux-calibrated using spectrophotometric standards (Oke 1990) and corrected for a telluric extinction, calculated independently each night. The spectra span from 3200–10000 Å with resolution of $\sim$ 1000.

Spectral types were determined by comparing spectra to template spectra of young stars, following Herczeg & Hillenbrand (2014). Veiling estimates were included in the spectral fits. The Hα line equivalent width was calculated by fitting a Gaussian profile to the line.

Near-infrared spectroscopy

28 optically faint targets were observed during 6 nights in visitor mode in August 2013 at the 4.2 William Herschel Telescope using the Long-slit Intermediate Resolution Infrared Spectrograph (LIRIS) instrument. We used the hr_k grism to obtain K-band spectra with a resolving power of R=3000 between 2 and 2.4 μm. K-band magnitudes ranged between 9 and 14 mags,

Table 9.4: *Optical/near infrared spectroscopy observations*

Date	Telescope	Instrument	Coverage	Resolving power
August 2012	WHT	ISIS	3500-9000 Å	R=1000
August 2013	WHT	LIRIS	2-2.4 μm	R=3000
June - August 2014	VLT	X-shooter	0.3-3.7 μm	R=8000

requiring integration times between 10 and 60 minutes. Telluric standards were observed once per hour. The LIRIS data are not yet reduced and therefore not included in this Chapter.

20 optically faint targets were observed in service mode in Summer 2014 at the Very Large Telescope using the X-shooter instrument as part of program 093.C-0757. X-shooter covers the entire optical and near infrared wavelength range between 0.3 and 3.7 μm with a resolving power of R=8000. The X-shooter data are not yet reduced and therefore not included in this Chapter.

9.3 Results

Table 9.5: *Comparison PACS photometry with previous estimates*

ID	$F_{70\mu m}$ (Jy)		$F_{100\mu m}$ (Jy)		$F_{160\mu m}$ (Jy)		Ref
	This study	Previous	This study	Previous	This study	Previous	
4	< 0.1	< 0.08	< 0.07	< 0.14	< 0.41	< 1.10	1
5	0.18 ± 0.05	0.15 ± 0.02	0.17 ± 0.03	0.17 ± 0.04	< 0.33	< 1.07	1
6	3.11 ± 0.31	3.08 ± 0.46	2.90 ± 0.29	2.82 ± 0.42	2.15 ± 0.25	2.32 ± 0.35	1
7	0.21 ± 0.04	< 0.28	0.21 ± 0.03	0.21 ± 0.01	< 0.31	< 0.32	2
9	< 0.65	0.60 ± 0.09	< 0.71	0.77 ± 0.12	< 1.06	0.98 ± 0.15	1
11	3.86 ± 0.39	3.88 ± 0.58	3.80 ± 0.38	3.63 ± 0.54	3.65 ± 0.37	3.86 ± 0.58	1
12	0.44 ± 0.05	0.38 ± 0.06	0.40 ± 0.05	0.36 ± 0.06	< 0.39	0.20 ± 0.03	1
13	< 0.11	< 0.04	0.14 ± 0.03	< 0.07	< 0.55	< 0.85	1
14	0.69 ± 0.08	0.68 ± 0.10	0.55 ± 0.06	0.57 ± 0.09	0.41 ± 0.07	< 0.30 ± 0.05	1
15	1.58 ± 0.16	1.61 ± 0.24	2.31 ± 0.23	2.19 ± 0.33	2.80 ± 0.28	2.74 ± 0.41	1
16	26.06 ± 2.92	25.91 ± 3.88	36.06 ± 3.9	32.32 ± 4.85	38.45 ± 6.0	27.3 ± 4.10	1
17	0.21 ± 0.05	< 0.25	0.25 ± 0.03	0.23 ± 0.01	0.30 ± 0.09	0.28 ± 0.05	2
24	0.17 ± 0.04	0.07 ± 0.02	0.11 ± 0.03	0.10 ± 0.02	< 0.09	< 0.13	3
25	< 0.34	0.11 ± 0.03	< 0.32	0.16 ± 0.04	< 0.38	< 0.23	3
26	< 0.26	0.10 ± 0.02	< 0.12	0.18 ± 0.04	< 0.02	< 0.19	3
27	0.61 ± 0.07	0.51 ± 0.13	0.80 ± 0.08	0.68 ± 0.17	0.96 ± 0.17	0.72 ± 0.18	3
179	1.23 ± 0.13	1.04 ± 0.26	1.41 ± 0.14	1.26 ± 0.31	1.69 ± 0.19	1.57 ± 0.39	3
185	0.21 ± 0.06	0.17 ± 0.04	0.24 ± 0.05	0.23 ± 0.06	< 0.91	0.29 ± 0.07	3
200	0.48 ± 0.06	0.36 ± 0.09	0.37 ± 0.05	0.37 ± 0.09	0.47 ± 0.15	0.26 ± 0.07	3

Refs. 1) Ribas et al. (2013), 2) Olofsson et al. (2013), 3) Bustamante et al. (2015)

9.3.1 Stellar parameters

Spectral types as derived from our observations and taken from the literature are given in Table 9.6. The observations of previously characterized stars resulted generally in the same spectral

types as derived before. Some of the WHT-ISIS targets did not show any lines and no spectral type could be determined: ID 32, 47, 101, 112, 114, 124, 125, 131, 164, 202 and 204, these SEDs were fit assuming a K7 star. ID 68, 80, 84, 104, 110, 119, 122 and 129 turned out to be giants, these SEDs were not further analyzed. For a handful of targets, the spectral type could not be determined to subtype accuracy. This paper presents new spectral types for 85 targets. For our final sample, spectral types are known for ~85% of our targets.

Spectral types are converted to the effective temperature $T_{\rm eff}$ using the scales in Kenyon & Hartmann (1995). The extinction A_V and stellar luminosity L_* (or stellar radius R_*, as $L_* = 4\pi R_*^2 \sigma T^4$) are fit simultaneously to the SEDs, assuming the distances listed at the bottom of Table 9.12. Kurucz models of stellar photospheres (Castelli & Kurucz 2004) are used as templates for the broadband emission. The 2MASS J-band and optical V and R band fluxes are taken as reference to constrain the fit, assuming no excess in these bands. When both V and R were missing, the extinction was estimated adopting $A_J = 1.53 \times E(J-K)$, where $E(J-K)$ is the observed color excess with respected to the expected photospheric color (Kenyon & Hartmann 1995), depending on its spectral type. The extinction law is parametrized as a function of wavelength assuming R_V=5.5 (Indebetouw et al. 2005) and scaled to the visual extinction A_V. The resulting values are listed in Table 9.6. Stellar masses are derived by interpolation of evolutionary models of Baraffe et al. (1998) in the position of the target on the HR diagram. For targets that could not be fit by the Baraffe models (which only include stars up to 1 $M_\odot$), masses were derived using the evolutionary models by Siess et al. (2000). Since uncertainties in stellar age are large, they are not tabulated here. We note that for the Serpens targets an alternative distance of 250 pc as used in previous work would often result in very high age estimates (>10 Myr), confirming that the 415 pc used here is likely more accurate (also demonstrated in Oliveira et al. 2009, 2013). For 10 targets no stellar mass could be derived, suggesting that their derived stellar properties are uncertain. Most of these are targets without known spectral type or late M stars.

The presence or absence of accretion can be assessed from the strength and shape of emission of the Hα and other optical lines (e.g. White & Basri 2003; Natta et al. 2006). Although a proper treatment of the accretion requires simultaneous fitting of extinction, luminosity and accretion through broadband spectroscopy (e.g. with X-shooter, Manara et al. 2014), as accretion also results in broadband UV/blue excess, the analysis in this study is limited to a simple designation of accretion by the width of the Hα line and we do not aim to quantify the accretion in terms of $M_\odot$ yr^{-1} due to the large uncertainties when deriving accretion from the line width only. Both the equivalent width EW[Hα] and the Hα 10% width have been used to distinguish between accretors and non-accretors, where the EW[Hα] cut-off depends on the spectral type (White & Basri 2003). Typically, a star is classified as an accretor if the Hα 10% width is >300 km s^{-1} (Natta et al. 2004), or if EW[Hα] > 3Å for an early-K star, > 10Å for a late-K star and > 20Å for an M star. Since other studies often only list the EW[Hα] values, our accretion designation is largely based on that. In recent years, several YSOs have been analyzed with broadband high resolution spectroscopy, including some of the targets in our sample (e.g. Alcalá et al. 2014; Manara et al. 2014). This accretion information is preferred above the derivation from the equivalent width as this method is more reliable, and those targets have been marked explicitly in Table 9.6. Accretion properties are known for 84% of our sample: about 64% of these targets are accreting, the remaining targets show little or no signs of accretion

Table 9.6: *Stellar parameters*

ID	SpT	T_{eff} (K)	A_V (mag)	L_* ($L_\odot$)	M_* ($M_\odot$)	EW[Hα] (Å)	FW10%[Hα][a] (km s^{-1})	Accretion[d] (Y/N)	Ref
1	K0	5250	2.0	1.34	1.1	-	400	Y	1,2
2	K5	4350	0.4	0.73	1.2	4.4	330	Y	3
3	M4	3370	2.4	0.14	0.3	35	330	Y	3
4	M3.5	3370	4.9	0.26	0.4	-	-	U	4
5	M4	3370	3.0	0.17	0.3	[b]	-	N	5
6	K2	4780	1.3	1.88	1.5	[b]	-	Y	6
7	M3.25	3470	5.7	0.16	0.4	200	-	Y	7
9	K0	5250	0.0	2.47	1.4	[b]	-	N	5
10	G5	5770	3.0	15.19	2.3	-	-	U	4
11	K2	4780	0.7	1.36	1.4	[b]	-	Y	6
12	K7	4060	3.4	0.41	1.0	[b]	-	Y	6
13	M0	3850	4.3	0.57	1.0	1	249	N	8
14	M0.5	3720	0.3	0.34	0.8	[b]	-	Y	6
15	K0	5250	2.4	4.99	2.0	[b]	-	Y	5
16	K5	4350	3.4	4.41	0.9	65	-	Y	9,4
17	M6	3050	6.9	0.17	0.1	43.6	-	Y	10
18	M2.5	3470	2.3	0.33	0.5	[b]	-	Y	6
20	K1	5080	0.9	1.35	1.2	-47	-	Y	11
21	F6	6360	1.4	23.58	2.3	[c]	-	Y	12
22	M3.5	3370	4.1	0.20	0.3	-0.4	-	N	13
23	M1.5	3580	0.1	0.38	0.6	-	375	Y	14
24	M4.5	3240	2.6	0.22	0.3	12.9	-	N	13
25	M4	3370	3.7	0.47	0.5	-	426	Y	14
26	M5	3240	1.0	0.19	0.3	-	201	Y	14
27	M0.5	3720	0.8	0.29	0.7	-	374	Y	14
28	M6	3050	0.0	0.22	0.1	-	189	Y	14
29	M5	3240	2.7	0.32	0.3	[b]	-	Y	6
30	K5	4350	0.8	0.05	1.0	0.1	-	N	13
31	M5.5	3050	4.9	1.51	-	-	-	U	13
32	-	4060	14.0	0.79	1.0	0.3	-	N	13
33	F4	6590	0.8	11.48	1.8	[c]	-	Y	12
34	M2	3580	5.7	0.12	0.5	-14.5	-	N	15
35	M1	3720	1.3	0.21	0.7	10.3	227	N	16
36	M6	3050	8.4	0.49	0.1	174.5	-	Y	13
38	K7	4060	0.0	1.08	1.2	[b]	-	Y	6
39	K5	4350	0.5	0.73	1.2	26.7	-	Y	13
40	K7	4060	4.6	0.88	1.2	-	470	Y	13,17
41	M2	3580	2.9	0.12	0.5	-	567	Y	17
43	M3	3470	4.2	0.38	0.5	88.7	-	Y	13
44	M2	3580	3.9	0.38	0.6	-	365	Y	17

Refs. 1) Alcala et al. (1995), 2) Schisano et al. (2009), 3) Lawson et al. (2004), 4) Luhman (2007), 5) Manara et al. (2015), 6) Manara et al. (2014), 7) Luhman & Muench (2008), 8) Spezzi et al. (2008), 9) Luhman (2004), 10) Comerón et al. (2004), 11) Silverstone et al. (2006), 12) Garcia Lopez et al. (2006), 13) This work, 14) Alcalá et al. (2014), 15) Sicilia-Aguilar et al. (2008), 16) Wahhaj et al. (2010), 17) Cieza et al. (2010), 18) Natta et al. (2006), 19) Brown et al. (2012a), 20) Wilking et al. (2005), 21) Oliveira et al. (2009), 22) White & Ghez (2001), 23) Rebull et al. (2010), 24) Salyk et al. (2013), 25) Nguyen et al. (2012), 26) Furlan et al. (2006), 27) Calvet et al. (2004), 28) Furlan et al. (2011), 29) Mooley et al. (2013), 30) Merín et al. (2010), 31) Cieza et al. (2007), 32) Cieza et al. (2012b), 33) Romero et al. (2012), 34) Rigliaco et al. (2015), 35) Kraus & Hillenbrand (2009), 36) Herczeg & Hillenbrand (2014), 37) Carpenter et al. (2008)

Notes. [a] We have reversed the signs of the width of the Hα line taken from Rebull et al. (2010) and Winston et al. (2009), as they list a negative value for emission and positive for absorption. [b] The accretion properties have been derived using a full X-shooter spectrum rather than only fitting the Hα line. [c] The accretion properties have been derived using other lines (e.g. Brγ). [d] 'Y' means accreting, 'N' means non-accreting', 'U' means unknown.

Table 9.6: *Stellar parameters*

ID	SpT	T_{eff} (K)	A_V (mag)	L_* ($L_\odot$)	M_* ($M_\odot$)	EW[Hα] (Å)	FW10%[Hα][a] (km s^{-1})	Accretion (Y/N)	Ref
45	K2	4780	5.8	2.07	1.5	[c]	-	Y	18
46	M0	3850	3.3	0.44	0.9	-	301	Y	13,17
47	-	4060	15.0	0.41	1.0	-0.6	-	N	13
48	M5.5	3050	5.8	0.38	0.1	[b]	-	Y	6
49	K5	4350	1.9	2.53	0.9	-	450	Y	13,17
50	M2	3580	2.9	0.38	0.6	[b]	-	Y	6
51	A0	9520	10.6	14.50	1.9	[c]	-	Y	19
52	K3	4730	2.9	1.46	1.4	[b]	-	Y	6
53	M4	3370	6.7	0.12	0.3	60.2	-	Y	13
54	G3	5830	5.5	6.50	1.7	[b]	-	Y	6
55	G	5830	6.0	1.76	1.2	8.4	-	Y	13
56	-	4060	11.2	0.04	-	-	-	U	
58	K8	3960	3.3	0.43	1.0	28.4	-	Y	13,20
59	M4	3370	5.2	0.20	0.3	-	159	N	13,17
60	M0	3850	3.7	0.28	0.9	[b]	-	Y	6
61	M2.5	3470	1.5	0.19	0.4	7.4	-	N	13
62	K5	4350	1.8	0.83	1.3	-	493	Y	13,17
63	K5	4350	2.6	0.73	1.2	44.5	-	Y	13
64	K5	4350	0.0	0.55	1.1	5.3	-	Y	13
65	F3	6740	0.8	10.71	1.7	-4.3	-	N	13
66	M5	3240	6.6	3.45	-	32	-	Y	13
67	-	4060	6.7	3.92	0.6	-	-	U	
68	M-GIANT	-	-	-	-	-	-	N	13
69	B9	10500	4.4	39.52	2.4	-9.8	-	N	13
70	G5	5770	5.2	3.23	1.4	5.8	-	Y	13
71	FG	6030	7.4	3.05	1.3	1.2	-	N	13
73	-	4060	14.4	7.14	0.7	-	-	U	
74	-	4060	10.6	1.53	1.2	-	-	U	
75	-	4060	13.2	3.92	0.6	-	-	U	
76	A0	9520	3.4	29.59	2.2	-9.2	-	N	13
77	F5	6440	4.5	4.48	1.4	-3.2	-	N	13
78	M5.5	3050	7.0	1.25	-	21.6	-	Y	13
79	A0	9520	1.8	23.97	2.2	-10.3	-	N	13
80	M-GIANT	-	-	-	-	-	-	N	13
81	FG	6030	10.8	4.30	1.4	-15.8	-	N	13
82	-	4060	9.3	0.02	1.0	-	-	U	
83	M4.5	3240	6.0	0.22	0.3	68.5	-	Y	13
84	M-GIANT	-	-	-	-	-	-	N	13
85	-	4060	14.0	0.12	1.0	-	-	U	
86	-	4060	14.9	0.12	1.0	-	-	U	
88	-	4060	11.0	2.83	1.0	-	-	U	
89	A6	8350	5.7	25.22	2.0	-5.7	-	N	13
90	-	4060	10.6	0.20	1.0	-	-	U	
91	-	4060	12.0	0.30	0.9	-	-	U	
92	-	4060	14.9	0.12	1.0	-	-	U	
93	A0	9520	12.4	32.63	1.0	-	-	N	13
94	-	4060	14.9	2.83	0.6	-	-	U	
95	-	4060	8.7	0.71	1.0	-	-	U	
96	-	4060	7.0	1.92	1.3	-	-	U	
97	-	4060	9.3	0.06	1.0	-	-	U	
98	-	4060	11.4	0.12	1.0	-	-	U	
99	A2	8970	2.7	16.85	1.9	-9.6	-	N	13
100	A7	7850	8.8	13.68	1.8	-6.6	-	N	13
101	-	4060	7.2	0.79	1.1	0.3	-	N	13
102	-	4060	19.8	0.35	1.0	-	-	U	
103	-	4060	15.0	0.88	1.2	-	-	U	
104	M-GIANT	-	-	-	-	-	-	N	13
105	FG	6030	8.7	3.86	1.4	1.7	-	N	13

Table 9.6: *Stellar parameters*

ID	SpT	T_{eff} (K)	A_V (mag)	L_* ($L_\odot$)	M_* ($M_\odot$)	EW[Hα] (Å)	FW10%[Hα][a] (km s^{-1})	Accretion (Y/N)	Ref
106	A7	7850	1.9	46.82	2.5	-6.6	-	N	13
107	M3	3470	3.4	0.38	0.5	4.8	-	N	13
108	-	4060	7.0	8.52	-	-	-	U	
110	M-GIANT	-	-	-	-	-	-	N	13
111	K2	4780	3.8	4.23	1.6	13.4	-	Y	13,21
112	-	4060	4.0	1.53	1.2	17.5	-	Y	13
113	FG	6030	5.2	0.19	-	-1.3	-	N	13
114	-	4060	7.1	8.52	-	-5.1	-	N	13
115	K7	4060	7.5	1.53	1.2	131.3	-	Y	13,21
116	FG	6030	6.6	2.68	1.0	-1.5	-	N	13
117	GK	5250	4.7	0.99	1.0	-5.3	-	N	13
118	M1	3720	1.0	0.21	0.7	9.3	-	N	13
119	M-GIANT	-	-	-	-	-	-	N	13
120	M2	3580	2.9	0.15	0.5	[b]	-	N	6
121	-	4060	3.8	0.12	1.0	-	-	U	
122	M-GIANT	-	-	-	-	-	-	N	13
123	B8	11900	4.0	52.20	1.0	-9.1	-	N	13
124	-	4060	11.0	0.63	1.1	-	-	U	
125	F4	6590	8.9	5.50	1.4	42.7	-	Y	13
126	M2	3580	1.0	0.21	1.0	88.6	-	Y	13,21
127	M1	3720	2.8	0.76	0.8	[b]	-	Y	6
128	K7	4060	3.8	1.41	1.2	10.9	273	Y	21
129	M-GIANT	-	-	-	-	-	-	N	13
130	K7	4060	4.3	0.20	0.8	38.0	-	Y	13
131	-	4060	5.1	0.63	1.1	9.8	-	Y	13
132	A2	8970	5.6	39.42	2.2	9.9	-	Y	13,21
133	K5	4350	0.7	1.04	1.4	7.4	-	Y	13,21
134	M2	3580	0.7	0.38	0.6	1.4	-	N	13
135	M1	3720	0.7	0.25	0.7	[b]	-	Y	6
136	K2	4780	0.8	1.88	1.5	9.5	-	Y	22
137	M2.5	3470	2.0	0.03	0.4	28.0	-	Y	13,23
138	M3	3470	5.6	0.29	0.5	4.2	-	N	13,23
139	K5	4350	5.1	0.08	-	18.2	-	Y	13,23
140	F2	6890	1.5	3.98	1.4	-5.5	-	N	23
142	A8	7580	0.7	34.37	2.3	[c]	-	Y	24
144	K1	5080	3.0	0.15	-	-1.1	-	N	13,23
145	M1	3720	0.5	0.44	0.8	-	348	Y	23,25
146	K3	4730	2.6	3.54	1.5	-1.1	-	N	23
147	M6	3050	3.0	0.02	0.1	17.3	-	N	23
148	M0	3850	0.6	0.51	0.9	11	-	Y	22
149	B8	11900	9.5	131.67	3.1	-	-	U	26
150	M4.5	3240	1.7	0.32	0.3	-	210	N	23
151	A0	9520	0.9	16.65	1.9	10	-	Y	23
152	K7	4060	1.1	0.79	1.1	-	180	N	23
153	G1	5945	2.8	17.11	2.3	[c]	-	Y	27
154	M0	3850	17.0	1.05	1.0	-	-	U	23
155	M1.25	3720	2.8	0.34	0.8	2.3	-	N	28
156	G5	5770	2.4	0.04	-	-2.4	-	N	13
157	M5	3240	3.7	0.44	0.2	21.8	-	Y	13
158	K0	5250	1.0	1.75	1.2	-1.2	110	N	16
159	A0	9520	1.6	112.53	3.1	[c]	-	Y	29,24
160	K4	4560	5.7	0.19	0.8	205	-	Y	13
161	K4	4560	5.7	0.19	0.8	17.6	-	Y	13,30
162	M0	3850	2.5	0.20	0.8	4.8	-	N	30
163	K6	4205	3.3	0.34	1.0	104.7	-	Y	13
164	-	4060	7.0	0.30	0.9	64.7	-	Y	13
165	K7	4060	7.1	0.35	1.0	4.3	-	N	30
166	FG	6030	5.4	3.86	1.4	-1.2	-	N	13

Table 9.6: *Stellar parameters*

ID	SpT	T_{eff} (K)	A_V (mag)	L_* ($L_\odot$)	M_* ($M_\odot$)	EW[Hα] (Å)	FW10%[Hα][a] (km s^{-1})	Accretion (Y/N)	Ref
167	K	4730	9.3	0.37	0.8	-2.9	-	N	13
168	M3	3470	3.1	0.16	0.4	130	504	Y	30
169	M4	3370	7.9	0.14	0.3	-5.7	-	N	13,30
171	M1	3720	2.6	0.69	0.8	11.5	-	N	31
172	M0.75	3720	0.7	0.17	0.7	-	280	N	32
173	G3	5830	3.0	12.75	2.2	[b]	-	Y	6
174	M0	3850	2.1	0.33	0.9	-	370	Y	13,32
175	M0	3850	3.2	0.16	0.8	-	350	Y	13,32
176	M4	3370	4.1	0.02	0.3	10.3	-	N	13
177	K7	4060	2.7	0.09	0.6	-	310	Y	32
178	-	4060	8.8	0.09	1.0	-	-	U	
179	K0	5250	1.3	1.34	1.1	-	532	Y	33
180	M0.75	3720	1.9	0.39	0.8	-	440	Y	33
181	K0	5250	4.8	2.22	1.3	-	360	Y	32
182	M2	3580	1.1	0.09	0.5	-	130	N	32
183	M2	3580	2.1	0.25	0.6	-	140	N	32
184	B9	10500	2.8	79.81	2.7	-	-	N	32
185	M5	3240	0.0	0.22	0.3	[b]	-	Y	14
186	M1	3720	0.0	0.25	0.7	82.6	416	Y	16
187	M0.5	3720	1.5	0.29	0.7	29.3	-	Y	23,34
188	M0	3850	1.0	0.33	0.9	99	-	Y	23
189	K5	4350	20.4	0.32	0.9	-	-	U	23
190	M2.25	3580	1.5	0.04	0.5	-	-	U	23
191	M6	3050	4.1	0.49	0.1	-	-	U	23
192	K6	4205	2.5	0.55	1.1	22	-	Y	23,35
193	M4.5	3240	4.3	0.29	0.3	114.6	-	Y	13
194	M5	3240	4.0	0.57	0.2	997.2	-	Y	23
195	M3.5	3370	8.6	0.26	0.4	-	-	U	23
196	M3.5	3370	3.7	1.34	0.3	-	-	N	36
197	K7	4060	2.5	1.65	1.2	-	458	Y	23,25
198	M1	3720	0.9	0.83	0.8	-	453	Y	25
200	M0	3850	0.5	0.57	1.0	24.2	-	Y	13
201	M3	3470	1.7	0.52	0.5	51.3	-	Y	13
202	-	4060	7.1	0.25	1.0	150.2	-	Y	13
203	-	4060	5.4	3.17	0.6	-	-	U	
204	-	4060	16.1	0.63	1.0	-	-	U	
301	M0.5	3720	0.7	0.50	0.8	0.2	311	N	30
303	-	4060	12.8	0.04	-	-	0	U	
307	-	4060	0.0	2.20	1.3	-	0	U	
309	K6	4205	1.3	0.34	1.0	[b]	-	Y	6
310	-	4060	0.5	0.02	-	-	0	U	
314	-	4060	4.6	0.25	0.9	-	0	U	
316	-	4060	16.1	0.63	1.0	-	0	U	
317	-	4060	2.2	2.35	1.0	-	0	U	
318	K1	5080	5.5	8.66	2.4	1.5	450	N	30
319	K7	4060	1.9	2.06	1.3	29.2	-	Y	13
321	F6	6360	4.4	9.96	1.7	-2.3	-	N	13,21
322	-	4060	2.3	0.71	1.1	-	0	U	
325	K3	4730	1.2	1.01	1.2	[b]	-	Y	6
326	M1	3720	0.1	0.29	0.7	-	185	N	23,25
329	K5	4350	0.3	0.83	1.3	[b]	-	Y	6
333	-	4060	0.0	2.35	1.3	-	0	U	
334	-	4060	2.7	0.01	-	-	0	U	
335	K6	4205	4.0	1.02	1.3	71.4	-	Y	13,30
348	G7	5630	0.6	3.27	1.4	-	-	U	37
349	K2	4780	0.7	0.92	1.2	[b]	-	Y	6
350	K2	4780	0.7	0.68	1.0	[b]	-	Y	6

9.3.2 Photometry

Herschel PACS surveys cover 92% of our targets. The derived fluxes and upper limits are listed in Table 9.13. For 152 targets at least one of the three wavelengths result in a detection. For 18 targets the emission is confused by cloud emission at all three wavelengths, for 27 only at 100 and 160 μm and for 62 targets only at 160 μm. For 25 of the targets without cloud confusion no flux is detected at any of the wavelengths.

The PACS 70 μm fluxes and upper limits are consistent with the MIPS-2 fluxes and upper limits. The PACS sensitivity is sometimes shallower than the MIPS-2, resulting in a higher upper limit. For some targets, a more thorough data reduction of the PACS data was performed in other work (Ribas et al. 2013; Olofsson et al. 2013; Bustamante et al. 2015). In Table 9.5 the derived fluxes and upper limits are compared. Our values are similar within errors with previous estimates, confirming the validity of our data reduction.

The submillimeter photometry resulted in a total of 34 detections and 39 upper limits, listed in Table 9.7 and 9.8. In addition, we have taken (sub)millimeter photometry from the literature (see Table 9.14). With 57 (sub)mm detections and 47 upper limits, about 50% of the targets in our sample have constraints at longer wavelengths.

Table 9.7: *JCMT photometry at 850 μm for our sample*

ID	Flux$_{850\mu m}$ (mJy)	ID	Flux$_{850\mu m}$ (mJy)
22	< 31	124	< 19
23	153	127	< 29
26	< 30	137	63 ± 18
29	31 ± 7	154	< 56
32	< 47	155	55 ± 18
36	73 ± 18	156	< 31 [a]
44	38 ± 11	161	< 115
47	< 50	163	< 117 [a]
56	< 59	166	167 ± 14
60	< 24	171	17 ± 6
63	95 ± 16	174	< 27
70	32 ± 11	178	222 ± 16
82	< 57	187	126 ± 18
86	< 107 [a]	189	93 ± 16
88	< 137 [a]	192	< 29
89	< 35	193	32 ± 9
92	< 79	196	69 ± 19
100	< 37	202	< 56
107	< 17 [a]	333	< 56
113	< 18		
120	< 21		

Notes. [(a)] The flux is contaminated by extended emission near the source position.

9.3.3 Disk parameters

Millimeter fluxes can be used to obtain a rough estimate of the disk mass assuming optically thin dust emission and a gas-to-dust ratio of 100. Disk masses $M_{\rm disk,mm}$ in our sample are

Table 9.8: *APEX photometry at 350 and 870 μm for our sample.*

ID	$F_{350\mu m}$ (Jy)	$F_{870\mu m}$ (mJy)	ID	$F_{350\mu m}$ (Jy)	$F_{870\mu m}$ (mJy)
1	2.4 ± 0.2	210 ± 20	40	< 0.7	< 20
2	-	< 40	43	-	< 18
6	0.69 ± 0.18		46	0.8 ± 0.2	164 ± 14
9	-	< 15	55	< 0.9	92 ± 6
10	-	< 20	58	-	< 18
11	2.4 ± 0.5		62	< 0.6	62 ± 9
14	-	24 ± 6	95	-	49 ± 11
15	4 ± 0.2	420 ± 50	98	-	63 ± 8
16	9.8 ± 2.4		99	-	360 ± 30 [a]
18	-	20 ± 6	132	-	109 ± 11 [a]
20	-	390 ± 10	200	-	< 40
22	< 0.3		203	-	55 ± 10 [a]
25	-	< 30	303	-	136 7
27	0.19 ± 0.04		307	-	123 ± 14
35	-	28 ± 4 [a]	316	-	98 ± 13
36	0.22 ± 0.06 [a]	< 30	321	-	< 20

Notes. [(a)] The flux is contaminated by extended emission near the source position.

calculated following the relations presented in Cieza et al. (2008) with standard assumptions and parameters:

$$M_{\rm disk} = 0.17 \left(F_{1.3mm}({\rm mJy}) \times \frac{d^2}{140{\rm pc}} \right) M_{\rm Jup} \tag{9.4}$$

$$M_{\rm disk} = 0.08 \left(F_{0.85mm}({\rm mJy}) \times \frac{d^2}{140{\rm pc}} \right) M_{\rm Jup} \tag{9.5}$$

with F_λ the flux at wavelength λ and d the distance to the star. Using this relation, disk masses of our sample range between <0.4 and 168 $M_{\rm Jup}$, and an average disk mass of 14 Jupiter masses, similar to large millimeter studies of disks (e.g. Andrews & Williams 2007a). However, these disk masses remain highly uncertain as the vertical structure, cavities and the stellar radiation field are not taken into account and the dust opacities and gas-to-dust ratio are uncertain.

Furthermore, we derive $L_{\rm disk}$ for each target by integrating over all data points after subtraction of the fitted stellar photosphere. The ratio $L_{\rm disk}/L_*$ is a measure of disk processing, as it traces the total amount of dust that is reprocessing stellar light. As disks become more tenuous, settle and eventually disappear, $L_{\rm disk}$ is expected to decline. The majority of the disks have $0.001 < L_{\rm disk}/L_* < 0.4$, as expected for flared disks. Disks with $L_{\rm disk}/L_* < 10^{-3}$ are generally considered as debris disks (e.g. Wahhaj et al. 2010). On the other hand, targets with $L_{\rm disk}/L_* >> 1$ are either embedded Class I objects or edge-on disks which are more difficult to analyze (Merín et al. 2010). ID178 has $L_{\rm disk}/L_* \sim 17$ and is thus removed from the analyzed sample.

Both $L_{\rm disk}/L_*$ and $M_{\rm disk,mm}$ are listed in Table 9.9. The final sample consists of 184 targets for which the SEDs will be analyzed.

9.4 Modeling

In order to determine the presence of a dust cavity and measure its size, the SEDs are modeled using the dust radiative transfer code RADMC-3D [3] (Dullemond & Dominik 2004). This code performs a Monte Carlo continuum radiative transfer calculation based on the input dust density profile and stellar photosphere, followed by raytracing of the SED. The model has a large number of input parameters and we have fixed as many as possible that are not important for our science goals. The model assumes a passive disk which reprocesses the stellar radiation field.

The modeling procedure consists of two steps: first using a rough grid with a broad range of parameters, followed by a finer grid for the specific stellar type. The modeling was performed blindly, without taking any results from previous SED modeling or imaging studies, for an uniform approach for each disk in this sample. In Section 9.5 the derived parameters are compared with previously found results.

9.4.1 Approach

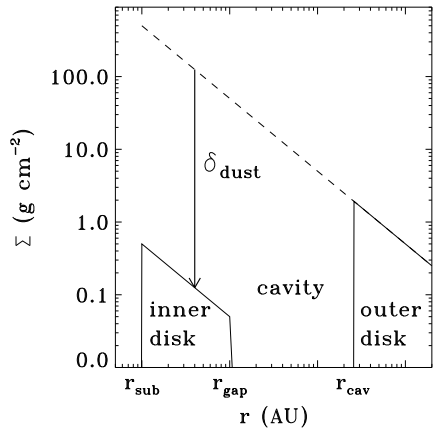

Figure 9.1: *Gas surface density profile used for the modeling, assuming a gas-to-dust ratio of 100.*

The disks are modeled using a large grid of models, computed by RADMC-3D. The model assumes an axisymmetric gas surface density profile, following a radial power-law

$$\Sigma_g(r) = \Sigma_c \left(\frac{r}{r_c}\right)^{-1} \tag{9.6}$$

with r_c the characteristic radius and a gas-to-dust ratio of 100. The outer radius is set to 200 AU and the inner radius to the sublimation radius $r_{\rm sub}$ with $r_{\rm sub} = 0.07(L_*/L_\odot)^{1/2}$, assuming a sublimation temperature of 1500 K (Dullemond et al. 2001). The dust density inside the cavity is parametrized by setting the density equal to zero between $r_{\rm gap}$ and $r_{\rm cav}$. The inner disk (between $r_{\rm sub}$ and $r_{\rm gap}$) is set by varying $\delta_{\rm dust}$ to fit the near infrared excess (see Figure

[3] http://www.ita.uni-heidelberg.de/~dullemond/software/radmc-3d/

9.1). The $r_{\rm gap}$ is fixed to 1 AU as it can not be constrained well by the SED. A full disk without a cavity is simulated by setting $r_{\rm cav} = r_{\rm gap}$.

The stellar photosphere in the model is described by its temperature and stellar luminosity, which has been fit independently together with the extinction. The disk is assumed to be flared, so that the vertical structure of the disk is described by

$$h(r) = h_c \left(\frac{r}{r_c}\right)^{\psi} \tag{9.7}$$

with h_c the scale height at r_c and ψ the flaring angle, which are both varied to fit the near and mid infrared part of the SED. As the scale height is degenerate with the cavity radius, the flaring angle is taken as a conservative value of either 1/7 or 2/7, following Chiang & Goldreich (1997). The derived cavity radius is thus likely a lower limit if the disk is flatter. With the inclusion of the *Herschel* fluxes, the scale height is better constrained than in previous SED modeling studies. Dust composition and settling is prescribed following Andrews et al. (2011), with a large and small dust grain population where the large grains have a lower scale height than the small grains. The inclination of the disks is taken as a constant of 30° and was not varied in the modeling, as only very high inclination angles (edge-on disks) result in a significant difference in the near infrared emission (and in addition, obscuration of the star). With our color criteria, edge-on disks are not expected to be included (Merín et al. 2010) and also the computation of the stellar masses from the stellar luminosities implies that most of the targets are not edge-on (although higher inclinations than 30° are still possible).

The five free parameters are thus $r_{\rm cav}$, $\delta_{\rm dust}$, Σ_c or disk mass, h_c and ψ, where $r_{\rm cav}$ is the main parameter of interest. The fitting was performed in two steps. First, a large grid of models with a broad range of disk parameters and a limited number of stellar parameters was fit to each SED. Second, each SED was fine-tuned individually, using the exact stellar photosphere and starting from the best fit from the broad grid. The disk grids per object have a large range of cavity radii (our main parameter of interest), in combination with a small range of scale heights and disk masses. In the fitting procedure, a χ^2 minimization was performed between the dereddened SED data points and the model SEDs. In the grid fitting, the data points were weighted by their excess above the stellar photosphere at each wavelength: fluxes at longer wavelengths got a larger weight than those in the optical and near infrared since the stellar photosphere is largely known from the extinction fitting. Uncertainties on the cavity radii are given in Table 9.9, based on fits with up to 10% variation in χ^2.

9.4.2 Results

Each SED can be fit to a disk model with or without a cavity. Table 9.9 presents the results of the fitting procedure. Figure 9.2 presents the distribution of hole sizes and disk masses (assuming a gas-to-dust ratio of 100) of the full sample, showing a broad distribution of both parameters. The disk masses obtained from the fit generally agree within a factor of 2-3 with the mass estimate from the millimeter flux. During the fit procedure it became clear that certain disks have really large cavities (>150 AU) but very low scale heights, which can not be well reproduced by our flared models. These disks are likely debris disks, as also suggested by their low $L_{\rm disk}/L_*$ values.

Table 9.9: *Results of disk fitting procedure and classification*

ID	r_{cav} (AU)	Σ_c (g cm^{-2})	$M_{disk,fit}$[a] (M_{Jup})	δ_{dust}	h_c	ψ	$M_{disk,mm}$[a] (M_{Jup})	L_{disk}/L_*	Classification[b]
1	140^{+10}_{-10}	7.0e-02	7.8	1.0e-02	0.10	1/7	3.7	0.467	ML
2	6^{+4}_{-4}	3.0e-03	1.1	1.0e-02	0.01	1/7	< 1.5	0.067	LS
3	10^{+2}_{-2}	3.0e-04	0.1	1.0e-04	0.01	1/7	-	0.038	LL
4	45^{+15}_{-5}	3.0e-04	0.1	1.0e-06	0.01	2/7	-	0.178	LL
5	30^{+50}_{-18}	3.0e-03	0.9	1.0e-01	0.05	2/7	-	0.195	LL
6	60^{+10}_{-10}	8.0e-02	20.9	1.0e-06	0.05	1/7	20.6	0.105	ML
7	8^{+2}_{-2}	3.0e-03	1.1	1.0e-02	0.15	1/7	-	0.685	LS
9	120^{+20}_{-10}	3.0e-04	0.0	1.0e-03	0.01	1/7	< 1.6	0.008	DD
10	190_{-10}	3.0e-04	0.0	1.0e-02	0.01	1/7	< 2.1	0.001	DD
11	30^{+10}_{-10}	5.0e-02	15.8	1.0e-04	0.05	2/7	32.8	0.329	ML
12	15^{+5}_{-5}	3.0e-03	1.0	1.0e-03	0.05	1/7	< 22.2	0.183	LL
13	190_{-10}	1.0e-02	0.2	1.0e-04	0.01	1/7	-	0.007	DD
14	10^{+4}_{-4}	3.0e-02	10.6	1.0e-04	0.05	1/7	2.5	0.201	ML
15	1^{+1}	1.5e-01	55.6	1.0e+00	0.03	1/7	43.9	0.083	MS
16	50^{+30}_{-49}	3.8e-01	106.1	1.0e-01	0.20	1/7	-	0.934	ML
17	15^{+15}_{-5}	3.0e-03	1.0	1.0e-06	0.05	2/7	-	0.172	LL
18	30^{+5}_{-5}	3.0e-03	0.9	1.0e-06	0.05	1/7	2.1	0.139	LL
20	1^{+3}	1.0e-01	37.1	1.0e+00	0.04	1/7	15.9	0.170	MS
21	110^{+10}_{-20}	6.0e-01	100.6	1.0e-01	0.10	1/7	216.0	0.366	ML
22	50^{+40}_{-10}	5.0e-03	1.4	1.0e-06	0.05	1/7	-	0.465	LL
23	60^{+10}_{-10}	1.0e-01	26.1	1.0e-06	0.05	2/7	25.0	0.152	ML
24	16^{+2}_{-4}	3.0e-03	1.0	1.0e-06	0.02	1/7	< 3.8	0.151	LL
25	4^{+4}_{-2}	3.0e-03	1.1	1.0e-04	0.01	1/7	-	0.100	LS
26	2^{+2}	3.0e-04	0.1	1.0e-02	0.05	1/7	< 5.0	0.307	LS
27	120^{+30}_{-20}	2.3e-02	3.4	1.0e-06	0.05	1/7	5.7	0.170	LL
28	2^{+2}	3.0e-04	0.1	1.0e-02	0.10	1/7	< 3.4	0.434	LS
29	70^{+40}_{-10}	6.0e-02	14.5	1.0e-08	0.02	1/7	2.8	0.136	ML
31	170^{+10}_{-20}	3.0e-04	0.0	1.0e-02	0.01	1/7	-	0.193	DD
33	80^{+10}_{-10}	1.5e-01	33.5	1.0e-01	0.05	1/7	49.6	0.233	ML
34	10^{+4}_{-4}	3.0e-04	0.1	1.0e-02	0.20	1/7	-	0.250	LL
35	2^{+2}	9.0e-02	33.2	1.0e-02	0.02	1/7	< 2.8	0.104	MS
36	1	1.5e-02	5.6	1.0e+00	0.05	1/7	6.7	0.337	NH
38	10^{+10}_{-2}	4.5e-01	159.2	1.0e-06	0.03	1/7	60.1	0.094	ML
39	16^{+4}_{-6}	1.0e-01	34.3	1.0e-04	0.03	1/7	16.8	0.117	ML
40	1	3.0e-03	1.1	1.0e+00	0.10	1/7	< 1.3	0.434	NH
41	1	3.0e-04	0.1	1.0e+00	0.05	1/7	< 1.3	0.107	NH
43	45^{+5}_{-20}	1.0e-03	0.3	1.0e-01	0.15	2/7	< 1.1	0.257	LL
44	4^{+2}_{-2}	7.0e-03	2.6	1.0e-04	0.05	1/7	2.4	0.146	LS
45	50^{+40}_{-20}	6.0e-02	16.8	1.0e-01	0.20	1/7	35.1	0.764	ML
46	20^{+10}_{-5}	3.0e-02	10.1	1.0e-06	0.05	1/7	10.5	0.114	ML
47*	1^{+1}	3.0e-03	1.1	1.0e+00	0.05	1/7	-	0.270	LS
48	8^{+6}_{-7}	3.0e-02	10.7	1.0e-02	0.05	1/7	-	0.350	MS
49	20^{+30}_{-10}	3.0e-03	1.0	1.0e-01	0.01	1/7	< 0.8	0.048	LL
50	2^{+2}	1.0e-03	0.4	1.0e-04	0.01	1/7	< 0.7	0.110	LS
51	120^{+10}_{-100}	2.0e-02	3.0	1.0e-04	0.10	1/7	11.5	0.310	LL

Notes. (*) Fit results are uncertain due to unknown spectral type. (a) Disk masses refer to the full disk mass, computed assuming a gas-to-dust ratio of 100. (b) NH = disks without holes, ML = massive disks with large holes, MS = massive disks with small holes, LL = low-mass disks with large holes, LS = low-mass disks with small holes, DD = low-mass disks with very low scale heights. See also definition in the text.

Table 9.9: *Results of disk fitting procedure and classification*

ID	r_{cav}	Σ_c	$M_{disk,fit}$ [a]	δ_{dust}	h_c	ψ	$M_{disk,mm}$ [a]	L_{disk}/L_*	Classification[b]
52	80^{+10}_{-20}	2.5e-02	5.6	1.0e-02	0.10	1/7	13.4	0.345	ML
53	1	3.0e-02	11.1	1.0e+00	0.01	1/7	-	0.054	NH
54	60^{+20}_{-15}	3.0e-02	7.8	1.0e-01	0.10	2/7	34.3	0.356	ML
55*	1	2.1e-02	7.8	1.0e+00	0.03	1/7	5.9	0.227	NH
56*	4^{+6}_{-2}	1.0e-02	3.6	1.0e-06	0.20	1/7	-	0.842	LS
58	1	8.0e-04	0.3	1.0e+00	0.15	1/7	< 1.1	0.418	NH
59	2^{+2}	3.0e-04	0.1	1.0e-04	0.01	1/7	-	0.115	LS
60	2^{+2}	3.0e-03	1.1	1.0e-06	0.01	2/7	< 1.5	0.062	LS
61	5^{+85}_{-3}	3.0e-04	0.1	1.0e-02	0.05	1/7	-	0.192	LS
62	1	1.2e-02	4.4	1.0e+00	0.05	1/7	4.0	0.238	NH
63	20^{+5}_{-5}	3.5e-02	11.7	1.0e-06	0.03	1/7	6.1	0.087	ML
64	70^{+20}_{-30}	5.0e-02	12.1	1.0e-04	0.08	1/7	20.4	0.359	ML
65	190_{-10}	3.0e-04	0.0	1.0e-06	0.01	1/7	-	0.001	DD
66	30^{+10}_{-26}	3.0e-03	0.9	1.0e-03	0.05	1/7	-	0.276	LL
67*	110^{+10}_{-10}	3.0e-04	0.1	1.0e-06	0.01	1/7	-	0.004	DD
69	190_{-10}	3.0e-04	0.0	1.0e-06	0.01	1/7	-	0.001	DD
70	80^{+30}_{-10}	6.0e-02	13.4	1.0e-04	0.03	1/7	8.3	0.077	ML
71*	180^{+10}_{-20}	3.0e-04	0.0	1.0e-04	0.01	1/7	-	0.003	DD
73*	190_{-10}	3.0e-02	0.6	1.0e-04	0.01	1/7	-	0.011	DD
74*	140^{+10}_{-100}	3.0e-02	3.4	1.0e-04	0.01	1/7	-	0.025	DD
75*	190_{-20}	3.0e-02	0.6	1.0e-04	0.01	1/7	-	0.013	DD
76	190_{-10}	3.0e-04	0.0	1.0e-06	0.01	1/7	-	0.002	DD
77	190_{-10}	3.0e-04	0.0	1.0e-06	0.01	1/7	-	0.002	DD
79	190_{-10}	3.0e-04	0.0	1.0e-06	0.01	1/7	-	0.000	DD
81*	70^{+30}_{-10}	3.0e-03	0.7	1.0e-02	0.05	1/7	-	0.129	LL
83	2^{+16}	3.0e-03	1.1	1.0e-04	0.01	2/7	-	0.053	LS
89	110^{+40}_{-10}	3.0e-05	0.0	1.0e-06	0.10	1/7	< 9.0	0.004	LL
91*	30^{+50}_{-25}	3.0e-02	9.5	1.0e-02	0.10	1/7	-	0.272	ML
94*	190_{-150}	3.0e-04	0.0	1.0e-04	0.10	1/7	-	0.010	LL
96*	60^{+50}_{-30}	3.0e-04	0.1	1.0e-04	0.05	1/7	-	0.039	LL
99	190_{-10}	6.0e+00	111.7	1.0e-10	0.01	2/7	91.8	0.025	ML
100	190_{-10}	6.0e-01	11.2	1.0e-06	0.01	1/7	< 9.4	0.016	ML
101*	5^{+85}_{-2}	1.0e-01	36.3	1.0e-06	0.01	1/7	-	0.045	MS
102*	45^{+115}_{-40}	3.0e-02	8.7	1.0e-01	0.20	1/7	-	0.702	ML
103*	40^{+5}_{-5}	3.0e-02	8.9	1.0e-01	0.10	1/7	-	0.338	ML
105*	190_{-10}	3.0e-04	0.0	1.0e-04	0.01	1/7	-	0.002	DD
106	190_{-10}	3.0e-04	0.0	1.0e-04	0.01	1/7	-	0.001	DD
107	70^{+40}_{-20}	3.0e-04	0.1	1.0e-06	0.10	1/7	< 4.4	0.047	LL
108*	180^{+10}_{-40}	3.0e-04	0.0	1.0e-02	0.05	1/7	-	0.011	LL
111	1	3.0e-01	111.2	1.0e+00	0.05	1/7	-	0.207	NH
112*	1	3.0e-03	1.1	1.0e+00	0.10	1/7	-	0.304	NH
113*	60^{+20}_{-20}	3.0e-03	0.8	1.0e-06	0.05	2/7	-	0.167	LL
114*	180^{+10}_{-130}	3.0e-03	0.1	1.0e-06	0.01	1/7	-	0.010	DD
115	5^{+35}_{-4}	5.0e-03	1.8	1.0e-01	0.20	1/7	< 12.4	0.889	LS
117*	60^{+40}_{-10}	3.0e-04	0.1	1.0e-06	0.01	1/7	-	0.019	LL
118	2^{+2}	3.0e-04	0.1	1.0e-02	0.15	1/7	-	0.397	LS
120	10^{+5}_{-8}	3.0e-03	1.1	1.0e-06	0.05	1/7	< 5.4	0.170	LL
124*	10^{+10}_{-5}	3.0e-03	1.1	1.0e-04	0.05	1/7	-	0.118	LL
125	50^{+10}_{-49}	3.0e-02	8.4	1.0e-01	0.20	1/7	-	0.927	ML
127	80^{+20}_{-10}	4.5e-02	10.1	1.0e-05	0.03	2/7	< 7.5	0.086	ML
128	25^{+45}_{-24}	3.0e-03	1.0	1.0e-02	0.05	1/7	-	0.086	LL

Table 9.9: *Results of disk fitting procedure and classification*

ID	$r_{\rm cav}$	Σ_c	$M_{\rm disk,fit}$ [a]	$\delta_{\rm dust}$	h_c	ψ	$M_{\rm disk,mm}$ [a]	$L_{\rm disk}/L_*$	Classification[b]
130	30^{+40}_{-25}	3.0e-04	0.1	1.0e-06	0.10	1/7	-	0.077	LL
131*	10^{+10}_{-5}	1.0e-02	3.5	1.0e-03	0.05	1/7	1.2	0.257	LL
132	180^{+10}_{-176}	5.0e-01	18.6	1.0e-04	0.05	1/7	27.8	0.146	ML
133	1	3.0e-02	11.1	1.0e+00	0.15	1/7	-	0.582	NH
134	190_{-10}	3.0e-04	0.0	1.0e-04	0.01	1/7	-	0.006	DD
135	4^{+2}_{-2}	9.0e-02	32.8	1.0e-06	0.05	1/7	16.8	0.121	MS
136	50^{+40}_{-10}	2.5e-02	7.0	1.0e-04	0.05	1/7	12.0	0.206	ML
137	4^{+2}_{-2}	4.0e-02	14.6	1.0e-01	0.20	2/7	5.1	1.236	MS
138	180^{+10}_{-20}	3.0e-03	0.1	1.0e-06	0.01	1/7	-	0.100	DD
139	2^{+2}	3.0e-03	1.1	1.0e-03	0.10	1/7	-	0.603	LS
140	190_{-10}	3.0e-04	0.0	1.0e-05	0.01	1/7	< 2.2	0.001	DD
142	25^{+15}_{-5}	3.0e-02	9.8	1.0e-01	0.05	1/7	29.4	0.203	ML
144	110^{+40}_{-10}	3.0e-03	0.5	1.0e-06	0.01	1/7	-	0.037	DD
145	1^{+1}	1.5e-02	5.6	1.0e+00	0.10	1/7	3.9	0.328	MS
146	190_{-10}	3.0e-04	0.0	1.0e-04	0.01	1/7	-	0.001	DD
147	6^{+9}_{-2}	3.0e-02	10.8	1.0e-01	0.05	2/7	-	0.426	MS
148	100^{+10}_{-30}	1.2e-02	2.2	1.0e-01	0.10	1/7	2.7	0.235	LL
149	10^{+8}_{-8}	3.0e-02	10.6	1.0e-06	0.03	1/7	51.0	0.153	ML
150	15^{+5}_{-5}	3.0e-04	0.1	1.0e-06	0.10	2/7	< 0.6	0.291	LL
151	190_{-10}	1.0e-04	0.0	1.0e-06	0.05	1/7	-	0.001	LL
152	150^{+20}_{-20}	3.0e-04	0.0	1.0e-04	0.01	1/7	< 0.7	0.003	DD
153	2^{+2}	3.0e-02	11.1	1.0e-02	0.10	1/7	44.8	0.385	MS
154	6^{+2}_{-2}	6.0e-02	21.7	1.0e-04	0.02	1/7	-	0.082	MS
155	50^{+10}_{-5}	1.2e-02	3.4	1.0e-06	0.05	1/7	4.4	0.141	LL
156	10^{+60}_{-5}	1.0e-02	3.5	1.0e-06	0.01	2/7	< 2.5	0.033	LL
157	1^{+4}	3.0e-03	1.1	1.0e+00	0.05	1/7	-	0.325	LS
158	190_{-10}	3.0e-04	0.0	1.0e-06	0.01	1/7	-	0.001	DD
159	1^{+5}	2.2e-02	8.2	1.0e+00	0.05	1/7	28.7	0.152	MS
160	1	1.0e-01	37.1	1.0e+00	0.20	1/7	-	1.191	NH
161	2^{+4}	8.0e-03	2.9	1.0e-03	0.20	1/7	< 29.4	0.785	LS
162	2^{+2}	1.5e-02	5.5	1.0e-06	0.05	2/7	3.4	0.321	MS
163	1^{+1}	3.0e-02	11.1	1.0e+00	0.20	1/7	< 29.9	0.978	MS
164*	1^{+3}	1.0e-03	0.4	1.0e+00	0.20	1/7	-	0.505	LS
165	8^{+4}_{-4}	1.0e-03	0.4	1.0e-04	0.02	1/7	< 0.8	0.052	LS
166*	140^{+20}_{-10}	1.5e-01	16.8	1.0e-01	0.15	1/7	42.5	0.424	ML
167*	8^{+42}_{-4}	3.0e-02	10.7	1.0e-04	0.05	1/7	-	0.238	MS
168	5^{+20}_{-3}	3.0e-03	1.1	1.0e-04	0.05	1/7	< 0.8	0.177	LL
169	2^{+2}	3.0e-04	0.1	1.0e-04	0.02	1/7	-	0.194	LS
171	1	1.2e-02	4.4	1.0e+00	0.10	1/7	4.4	0.343	NH
172	2^{+1}	3.2e-02	11.8	1.0e-06	0.10	1/7	7.9	0.384	MS
173	120^{+10}_{-20}	3.0e-01	44.7	1.0e-04	0.05	1/7	53.6	0.331	ML
174	18^{+10}_{-6}	9.0e-02	30.5	1.0e-06	0.05	1/7	< 22.2	0.257	ML
175	4^{+8}_{-2}	1.5e-03	0.5	1.0e-04	0.15	2/7	0.8	0.542	LS
176	2^{+2}	3.0e-03	1.1	1.0e-06	0.05	2/7	-	0.195	LS
177	25^{+10}_{-10}	6.0e-03	2.0	1.0e-06	0.01	1/7	< 0.4	0.019	LL
179	1^{+59}	2.0e-02	7.4	1.0e+00	0.05	1/7	9.2	0.141	MS
180	14^{+4}_{-4}	3.0e-04	0.1	1.0e-06	0.05	1/7	< 1.8	0.071	LL
181	6^{+12}_{-5}	3.0e-03	1.1	1.0e+00	0.01	1/7	< 0.6	0.067	LS
182	2^{+23}	1.0e-02	3.7	1.0e-04	0.01	1/7	-	0.044	LS
183	4^{+1}_{-2}	3.0e-03	1.1	1.0e-06	0.05	1/7	< 0.8	0.119	LS
184	160^{+20}_{-10}	1.0e-04	0.0	1.0e-04	0.01	1/7	< 1.5	0.003	DD

Table 9.9: *Results of disk fitting procedure and classification*

ID	r_{cav}	Σ_c	$M_{disk,fit}$[a]	δ_{dust}	h_c	ψ	$M_{disk,mm}$[a]	L_{disk}/L_*	Classification[b]
185	1	1.0e-02	3.7	1.0e+00	0.12	1/7	< 9.4	0.582	NH
186	1	3.0e-04	0.1	1.0e+00	0.10	2/7	-	0.274	NH
187	4^{+2}_{-2}	2.7e-02	9.9	1.0e-01	0.20	1/7	10.0	1.076	MS
188	1	5.0e-03	1.9	1.0e+00	0.15	1/7	2.6	0.452	NH
189	40^{+80}_{-30}	3.0e-02	8.9	1.0e-01	0.07	1/7	-	0.302	ML
190	2^{+2}	1.5e-02	5.5	1.0e-04	0.05	1/7	1.4	0.147	MS
191	2^{+2}	1.0e-03	0.4	1.0e-02	0.05	1/7	-	0.449	LS
192	25^{+10}_{-10}	3.0e-03	1.0	1.0e-02	0.20	1/7	< 2.3	0.617	LL
193	10^{+10}_{-8}	8.0e-03	2.8	1.0e-04	0.05	1/7	2.6	0.125	LL
194	10^{+2}_{-5}	7.0e-02	24.8	1.0e-05	0.02	1/7	2.3	0.157	ML
195	2^{+2}	3.0e-04	0.1	1.0e-02	0.05	1/7	-	0.264	LS
196	2^{+2}	1.1e-02	4.1	1.0e-04	0.05	1/7	5.5	0.219	LS
197	1	3.0e-02	11.1	1.0e+00	0.03	1/7	10.4	0.114	NH
198	90^{+50}_{-10}	2.0e-02	4.1	1.0e-02	0.15	1/7	7.2	0.314	LL
200	1	2.0e-02	7.4	1.0e+00	0.10	1/7	< 6.5	0.397	NH
201	1^{+3}	7.0e-02	25.9	1.0e+00	0.05	1/7	-	0.340	MS
203*	2^{+98}	4.0e-02	14.7	1.0e-01	0.10	2/7	-	0.900	MS
301	2^{+2}	3.0e-02	11.1	1.0e-02	0.05	1/7	-	0.242	MS
303*	4^{+6}_{-2}	7.0e-02	25.5	1.0e-04	0.20	2/7	-	2.820	MS
307*	160^{+10}_{-20}	4.5e-02	3.4	1.0e-06	0.05	2/7	-	0.107	LL
309	10^{+2}_{-2}	3.0e-02	10.6	1.0e-04	0.02	1/7	-	0.066	ML
310*	20^{+60}_{-14}	6.0e-01	201.1	1.0e-02	0.20	2/7	-	1.477	ML
314*	20^{+10}_{-10}	1.0e-02	3.4	1.0e-06	0.05	1/7	-	0.146	LL
318	70^{+30}_{-10}	3.0e-04	0.1	1.0e-02	0.05	2/7	-	0.048	LL
319	1^{+17}	3.0e-03	1.1	1.0e+00	0.05	1/7	-	0.116	LS
321	190_{-10}	3.0e-03	0.1	1.0e-05	0.01	1/7	< 5.1	0.018	DD
322*	70^{+10}_{-10}	3.0e-01	72.6	1.0e-08	0.05	1/7	-	0.225	ML
325	80^{+40}_{-35}	1.3e-01	29.0	1.0e-01	0.05	1/7	32.8	0.159	ML
326	6^{+2}_{-2}	3.0e-02	10.8	1.0e-06	0.10	1/7	-	0.460	MS
329	30^{+10}_{-5}	1.6e-01	50.6	1.0e-04	0.05	2/7	51.2	0.211	ML
333*	50^{+30}_{-10}	1.0e-02	2.8	1.0e-05	0.10	1/7	-	0.533	LL
334*	8^{+112}_{-7}	3.0e-01	107.3	1.0e-01	0.20	2/7	-	1.528	MS
335	2^{+8}_{-1}	3.0e-01	110.6	1.0e-01	0.05	2/7	-	0.280	MS
348	20^{+10}_{-8}	3.0e-03	1.0	1.0e-01	0.10	1/7	-	0.328	LL
349	160^{+10}_{-10}	3.0e-01	22.3	1.0e-04	0.05	1/7	8.9	0.201	ML
350	10^{+2}_{-2}	6.0e-02	21.2	1.0e-06	0.03	1/7	-	0.228	ML

Figures 9.12 to 9.16 present the SEDs with the best fitting models overlaid. The SEDs are grouped into 5 different classifications:

- NH: Disks without holes (r_{cav}=1 AU)
- ML: Massive disks with large holes (r_{cav} >10 AU, $M_{disk} > 5M_{Jup}$)
- MS: Massive disks with small holes (r_{cav} <10 AU, $M_{disk} > 5M_{Jup}$)
- DD: Low-mass disks with large holes and very low scale heights (r_{cav} >100 AU, $M_{disk} < 5M_{Jup}$, $h_c \sim 0.01$)

- LL: Low-mass disks with large holes
  ($r_{\rm cav}$ >10 AU, $M_{\rm disk} < 5 M_{\rm Jup}$, $h_c > 0.01$)
- LS: Low-mass disks with small holes
  ($r_{\rm cav}$ <10 AU, $M_{\rm disk} < 5 M_{\rm Jup}$)

For the disks classified as NH (no hole), we have excluded the targets that could be fit with a cavity >1 AU within the 10% χ^2 limit. A large fraction of the disks (~23%) falls in the ML category of large holes in massive disks. It turns out that several of these disks are indeed the famous, bright disks with large inner holes known from imaging surveys (Andrews et al. 2011; Williams & Cieza 2011), confirming the strength of our SED modeling, even if rather simple. The new targets in the ML, MS and some in the LL groups are promising disks for follow up observations with ALMA. Excluding the DD and NH disks, a total of 133 targets (72% of our analyzed sample) can be labeled as disks with cavities, transition disks. More than half of these (~ 70 targets) are new transition disks; about 40 had been imaged or modeled before and another 20 had been recognized as a possible transition disk. Of the new transition disks, two thirds have a known spectral type.

9.5 Discussion

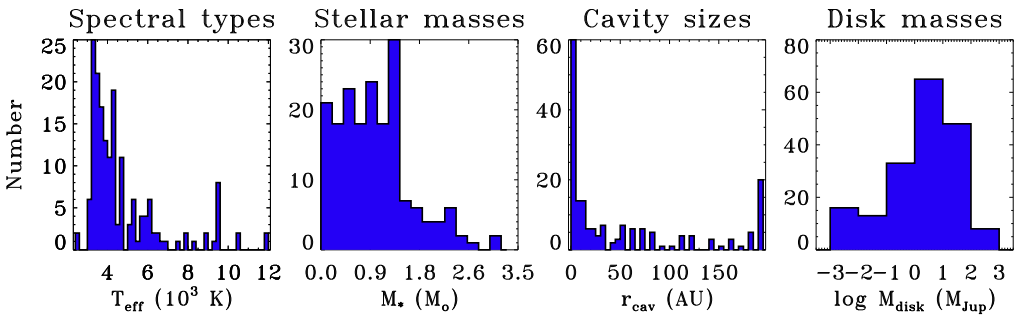

Figure 9.2: *Distribution of spectral types, stellar masses, cavity sizes and disk masses in this study. The disk mass is calculated assuming a gas-to-dust ratio of 100.*

The SED modeling has confirmed the presence of cavities in a large unbiased sample of transition disks. At least 72% of the sample could be modeled as a disk with a cavity, including about 110 new transition disks that had not been identified as transition disk before.

9.5.1 Comparison of cavity radii with literature values

In order to quantify the quality of our fitting, the fit results for the cavity size are compared with values from the literature from both SED modeling and resolved millimeter imaging in Table 9.10 for the targets where this information is available. The values generally agree well within a factor of two with previously derived parameters. Especially the similarity to the imaging results is encouraging: this implies that a large number of our new targets are suitable for resolved imaging. Exceptions for the imaging targets are T Cha, RY Tau and AB Aur. For T Chathe overestimate of the cavity size could be caused by the assumed low inclination: imaging has shown that the inclination is in reality ~ 67° so close to edge-on (Huélamo et al.

Table 9.10: *Comparison cavity radii with literature values.*

ID	Name	r_{cav}^{here}	r_{cav}^{lit}	Type[a]	Ref	ID	Name	r_{cav}^{here}	r_{cav}^{lit}	Type[a]	Ref
1	TCha	140^{+10}_{-10}	19	I	1	51	IRS48	120^{+10}_{-100}	60	I	13
3	RECX5	10^{+2}_{-2}	33	M	2	52	DoAr44	80^{+10}_{-20}	30	I	10
4	CHXR22E	45^{+15}_{-5}	7	M	3	54	SR21	60^{+20}_{-15}	36	I	8
6	CSCha	60^{+10}_{-10}	38	M	4	60	oph62	2^{+2}	3	M	6
9	T54	120^{+20}_{-10}	37	M	3	64	J160421	70^{+20}_{-30}	80	I	14
10	T21	190_{-10}	146	M	3	120	J182911	10^{+5}_{-8}	8	M	6
11	SZCha	30^{+10}_{-10}	29	M	3	127	Serp127	80^{+20}_{-10}	25	M	6
12	T35	15^{+5}_{-5}	15	M	3	128	J182935	25^{+45}_{-23}	7	M	6
14	T56	10^{+4}_{-4}	18	M	3	135	DMTau	4^{+2}_{-2}	18	I	10
15	CRCha	1^{+1}	10	M	4	136	UXTauA	50^{+40}_{-10}	25	I	10
18	T25	30^{+5}_{-5}	8	M	3	142	MWC758	25^{+15}_{-5}	73	I	10
21	HD142527	110^{+10}_{-20}	100	I	5	148	IPTau	100^{+10}_{-30}	2	M	4
24	Lup60	16^{+2}_{-4}	3	M	6	153	RYTau	2^{+2}	$26^{(b)}$	I	15
27	Sz91	120^{+30}_{-20}	97	I	7	159	ABAur	1^{+4}	115	I	16
29	Sz84	70^{+40}_{-10}	55	M	6	161	ASR118	2^{+4}	1	M	6
33	HD135344	80^{+10}_{-10}	46	I	8	165	J034227	8^{+4}_{-4}	5	M	6
35	Sz76	2^{+2}	1	M	9	168	J034434	5^{+20}_{-3}	3	M	6
38	RXJ1615	10^{+10}_{-2}	30	I	10	169	IC348LRL190	2^{+2}	5	M	6
39	V4046Sgr	16^{+4}_{-6}	29	I	11	173	LkH-alpha330	120^{+10}_{-20}	68	I	10
45	SR24S	50^{+40}_{-20}	30	I	10	309	TWHya	10^{+2}_{-2}	4	M	17
46	RXJ1633	20^{+10}_{-5}	27	I	12	325	LkCa15	80^{+40}_{-35}	50	I	10
48	WSB60	8^{+6}_{-6}	15	I	10	326	CoKu-Tau-4	6^{+2}_{-2}	10	M	18
50	J162245	2^{+2}	1	M	6	329	GMAur	30^{+10}_{-5}	20	I	10

Refs. 1) Huélamo et al. (2015), 2) Bouwman et al. (2010), 3) Kim et al. (2009), 4) Espaillat et al. (2011), 5) Fukagawa et al. (2013), 6) Merín et al. (2010), 7) Canovas et al. (2015), 8) Brown et al. (2009), 9) Padgett et al. (2006), 10) Andrews et al. (2011), 11) Rosenfeld et al. (2013), 12) Cieza et al. (2012a), 13) van der Marel et al. (2013), 14) Mathews et al. (2012), 15) Isella et al. (2010a), 16) Piétu et al. (2005), 17) Andrews et al. (2012), 18) D'Alessio et al. (2005)

Notes. [a] M = derived from SED modeling, I = derived from millimeter imaging. [b] This value is not a real cavity size, but a transition radius: the disk was fit with a surface density profile that radially increases and decreases, peaking at 26 AU.

2015), affecting the near infrared emission from the inner disk. Also their flaring angle is lower than ours. For RY Tau, the cavity radius found by imaging is not defined in the same way as here: it is the peak of the surface density, assuming a surface density that first increases and then decreases with radius (Isella et al. 2010a). Therefore, the values can not be compared directly. For AB Aur, only a very small hole of at most 2 AU can be fit with our models, while millimeter imaging has revealed a large cavity of 115 AU at 1.4mm, with a complex, possibly spiral-arm structure (Piétu et al. 2005; Tang et al. 2012). It remains unclear what the reason is for this discrepancy between the SED and the millimeter image. For the comparison with SED modeling there are large discrepancies for CHXR22E, T54, CR Chaand IP Tau. These targets were not modeled with a full radiative transfer code but a parametrized temperature profile and optically thin dust emission inside the cavity rather than an inner disk (Kim et al. 2009; Espaillat et al. 2011), so the results can not be compared directly.

9.5.2 Binaries

Some transition disks can be explained as circumbinary disks due to the dynamical interaction between the disk and a stellar companion. The cavity size is expected to be ~2 times as large as the binary separation (Artymowicz & Lubow 1996). The fraction of the transition disks in

our sample for which binarity has been studied is limited, but for those targets where spatially resolved information is available from the literature (either detections or upper limits), the properties are listed in Table 9.11, together with the cavity sizes found in this study.

Table 9.11: *Multiplicity properties*

ID	Separation (arcsec)	Separation (AU)	r_{cav} (AU)	Ref	ID	Separation (arcsec)	Separation (AU)	r_{cav} (AU)	Ref
1	0.062	6.7	140^{+10}_{-10}	1	60	<0.1	<12	2^{+2}	9
4	<0.1	<16	45^{+15}_{-5}	2	62	<0.1	<12	1	9
5	<0.1	<16	30^{+50}_{-18}	2	63	<0.13	<16	20^{+5}_{-5}	10
6	-	4	60^{+10}_{-10}	3	64	<0.01/>0.3	<1.5/>50	70^{+20}_{-30}	11
7	<0.75	<120	8^{+2}_{-2}	4	134	<0.13	<18	190_{-10}	12
9	0.25	40	120^{+20}_{-10}	2	135	>0.03	>4	4^{+2}_{-2}	13
10	0.14	22	190_{-10}	2	136	>0.03	>4	50^{+40}_{-10}	13
11	<0.07/5.122	<11/800	30^{+10}_{-10}	2	140	<0.1	<14	190_{-10}	14
12	<0.07	<11	15^{+5}_{-5}	2	149	0.06/4.1	8/560	10^{+8}_{-8}	15
14	<0.07	<11	10^{+4}_{-4}	2	150	<0.1	<14	15^{+5}_{-5}	14
15	<0.08	<13	1^{+1}	2	152	<0.1	<14	150^{+20}_{-20}	14
16	<0.12	<19	50^{+30}_{-49}	2	153	>0.03	>4	2^{+2}	13
17	<0.75	<120	15^{+15}_{-5}	4	162	<0.1	<25	2^{+2}	14
18	<0.08	<13	30^{+5}_{-5}	2	172	<0.1	<25	2^{+1}	14
21	0.088	13	110^{+10}_{-20}	5	174	<0.1	<45	18^{+10}_{-6}	14
23	<0.7	<140	60^{+10}_{-10}	6	175	0.83	116	4^{+8}_{-2}	14
24	<0.1	<20	16^{+2}_{-4}	7	177	1.2	168	25^{+10}_{-10}	14
25	<0.8	<160	4^{+4}_{-2}	6	179	<0.1	<15	1^{+59}	7
27	<0.1	<20	120^{+30}_{-20}	7	180	0.5	72	14^{+4}_{-4}	7
28	<0.1	<20	2^{+2}	7	181	<0.1	<25	6^{+12}_{-5}	14
33	<0.1	<14	80^{+10}_{-10}	8	182	<0.1	<25	2^{+23}	14
40	<0.1	<12	1	9	183	<0.1	<25	4^{+1}_{-2}	14
41	<0.1	<12	1	9	184	<0.1	<25	160^{+20}_{-10}	14
43	<0.13	<16	45^{+5}_{-20}	10	191	0.22	30	2^{+2}	16
44	<0.1	<12	4^{+2}_{-2}	9	200	<0.06	<12	1	6
46	<0.1	<12	20^{+10}_{-5}	9	309	<0.1	<5	10^{+2}_{-2}	8
47	<0.13	<16	1^{+1}	10	318	-	1.5	70^{+30}_{-10}	17
48	<0.1	<12	8^{+6}_{-7}	8	319	0.638	80	1^{+17}	10
49	0.33	41	20^{+30}_{-10}	9	325	>0.03	>4	80^{+40}_{-35}	13
50	0.54	68	2^{+2}	9	326	0.053	8	6^{+2}_{-2}	18
58	<0.13	<16	1	10	329	>0.03	>4	30^{+10}_{-5}	13
59	<0.1	<12	2^{+2}	9					

Refs. 1) Huélamo et al. (2011), 2) Lafrenière et al. (2008), 3) Guenther et al. (2007), 4) Comerón (2012), 5) Biller et al. (2012), 6) Ghez et al. (1997), 7) Romero et al. (2012), 8) Vicente et al. (2011), 9) Cieza et al. (2010), 10) Ratzka et al. (2005), 11) Kraus et al. (2008), 12) Kohler & Leinert (1998), 13) Pott et al. (2010), 14) Cieza et al. (2012b), 15) Leinert et al. (1997), 16) Biller et al. (2011), 17) Loinard et al. (2008), 18) Ireland & Kraus (2008)

Although for a handful of targets the cavity can indeed be explained by a binary companion, for the bulk of the disks the limits are not sufficient to exclude circumbinary disks. Previous binary studies of transition disks already revealed that most of the sharp cavities are not due to binary systems (Pott et al. 2010; Vicente et al. 2011).

9.5.3 Accretion

By combining the outcome of the SED modeling with our information on accretion, the possibility of photoevaporation as origin of the cavities can be checked. According to photoevaporation models (e.g. Alexander et al. 2006a), UV photons from the star heat and ionize the

gas in the disk; beyond a critical radius, the thermal velocity of the ionized gas exceeds its escape velocity and the material is dissipated as a wind. During the lifetime of the disk, the accretion rate is expected to gradually decrease: when the rate drops below the photoevaporation rate, the outer disk can no longer resupply the inner disk with material and an inner hole is formed. This process is called photoevaporative clearing, and transition disks created by this mechanism are expected to have no or very low accretion. Clearing of a gap by a planet and photoevaporation could also happen simultaneously (e.g. Rosotti et al. 2013), making the distinction not purely measurable by accretion alone. Figure 9.3 shows the number of objects in each class that are accreting/non-accreting. The accretors are dominated by disks without holes and massive disks with large holes, which are likely transition disks with a cavity due to clearing by a companion. The non-accretors are dominated by the low-scale height low-mass disks (DD), confirming that they are likely debris disks. The non-accreting low-mass disks are possibly disks where the hole is caused by photoevaporative clearing, but as there are several low-mass accreting disks as well there is no general trend for the low-mass disks. The non-accreting disk without a hole (ID171) is an outlier, but the equivalent width of this target is on the edge of accreting/non-accreting, probably due to the ubiquitous variable accretion (Mendigutía et al. 2012), and should thus have been classified as an accretor.

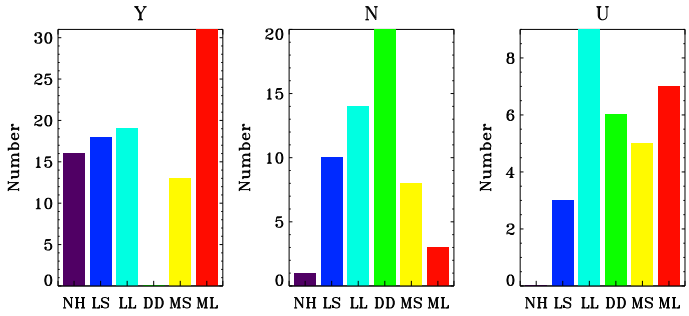

Figure 9.3: *Comparison of accretion properties from Table 9.6 with disk hole parameters: Y means accreting, N means non-accreting, U means unknown.*

9.5.4 Evaluation of color criteria

Considering the high success rate of new transition disks found in the sample in this study, it is now possible to re-evaluate the criteria used to select the targets. Figure 9.4 presents the the resulting classifications from our SED modeling for each of the four color selection criteria.

From Figure 9.4 it is clear that the disks without holes are most dominant in the B criteria, but overall at a low fraction. The L criteria are particularly biased towards the low scale height disks and low-mass disks with large holes. Massive disks with large holes are found in all colors. Evaluating the M10 criteria directly in the color-color plot, the DD disks fall outside the A and B range. A small amount of disks with holes falls outside the range of the A, B criteria (these are targets from the literature), generally with a shallower 8-24 μm slope.

9.5.5 Comparison with Cieza survey

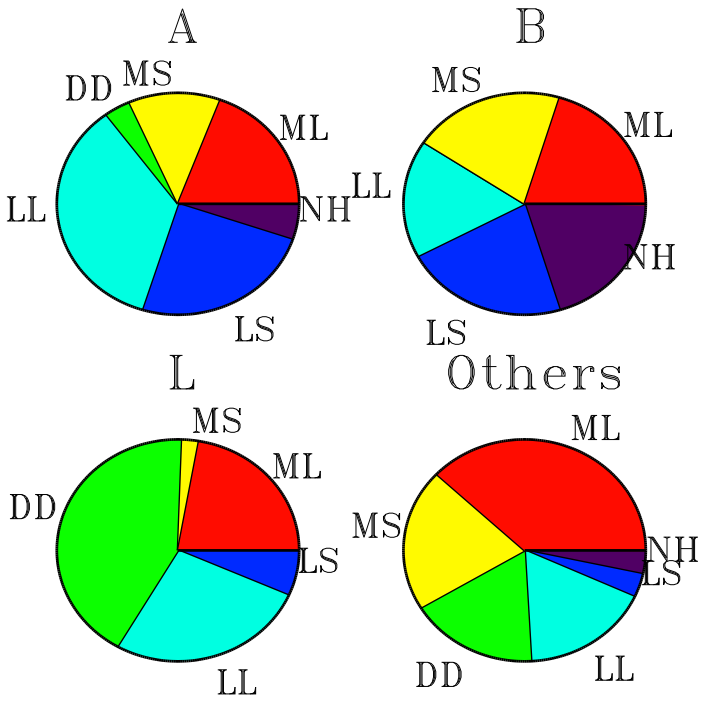

Figure 9.4: *Evaluation of the color criteria (Region A, B and L colors) vs the outcome of the SED modeling.*

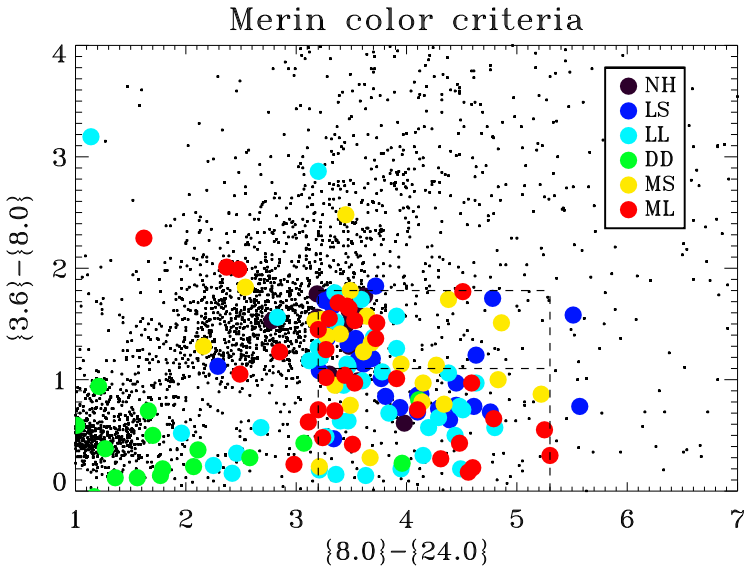

Figure 9.5: *Evaluation of the color criteria (A and B) vs the outcome of the SED modeling. The filled symbols are the targets analyzed in this study, the dots are all YSOs in the c2d, GB and Taurus catalogs. The dashed lines mark the Region B (top) and Region A (bottom) criteria.*

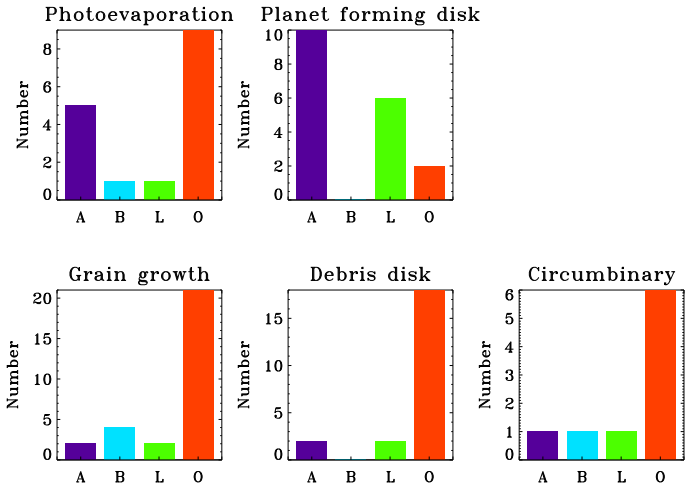

Figure 9.6: *Comparison of the categorization by the Cieza et al. studies with the color criteria used in this study applied to the Cieza sample.*

A previous large survey of transition disk candidates was performed by Cieza et al. (2010, 2012b) and Romero et al. (2012), who selected a sample of candidates using their own color criteria. Rather than SED modeling, they apply criteria based on a range of observables (disk mass, $L_{\rm disk}/L_*$, accretion, multiplicity, infrared spectral slope $\alpha_{\rm excess}$ and the wavelength where the disk emission starts to dominate, $\lambda_{\rm turnoff}$) to determine the origin of the dust deficit in their disks: circumbinary disk, photoevaporative clearing, debris disk, grain growth or planetary clearing.

Of particular interest are their planet-forming disks, which are massive, accreting disks with sharp cavities ($\alpha_{\rm excess} > 0$). Their final target list is compared with our sample, and the colors used for our color criteria have been derived for all their targets. Note that 27 of their 92 targets were already present in our sample, either selected by the color criteria or by their classification in the literature. Figure 9.6 shows how their categorization overlaps with our color criteria for these 27 targets and Figure 9.7 shows the inital color selection of Cieza et al. ([3.6]-[4.5]<0.25, [3.6]-[24.0]>1.5) in comparison with the outcome of our classification.

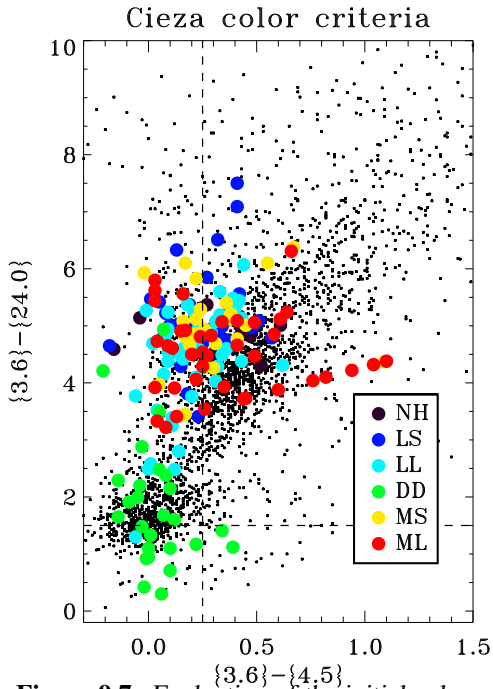

Figure 9.7: *Evaluation of the initial color criteria by the Cieza survey vs the outcome of our SED modeling. The filled symbols are the targets analyzed in our study, the dots are all YSOs in the c2d, GB and Taurus catalogs. The dashed lines mark the regions: the upper left quartile are the transition disks according to Cieza, the lower left quartile are diskless stars.*

Finally, Figure 9.8 shows how the classification of Cieza et al. compares with our classification for our targets.

Our A and L color criteria are clearly favored in the planet forming disks, while many of the less interesting disks from our perspective (grain growth, debris disks) fall in category, 'O', outside our color criteria. Several of the photoevaporation disks also follow the A criteria. This comparison confirms that our color criteria are good at selecting disks with sharp inner cavities. Inspection of the initial color criteria that Cieza et al. used for selecting targets shows only 50% of our disks with holes fall within these criteria. The DD targets fall in the same quartile as the diskless stars, as expected. Looking at the comparison of the Cieza classification with the outcome of our SED modeling in Figure 9.8, planet forming disks fall mostly within the class of massive disks with large cavities, while photoevaporation and debris disks are mostly consistent with low-mass disks. Neither of this is a surprise, considering the categorization of Cieza et al. (2010). Disks without holes all fall within the category of grain-growth disks. On the other hand, several other disks in the grain-growth category could be fit with a disk including a cavity. Note that circumbinary disks are not well-constrained for most of our sample and therefore not included.

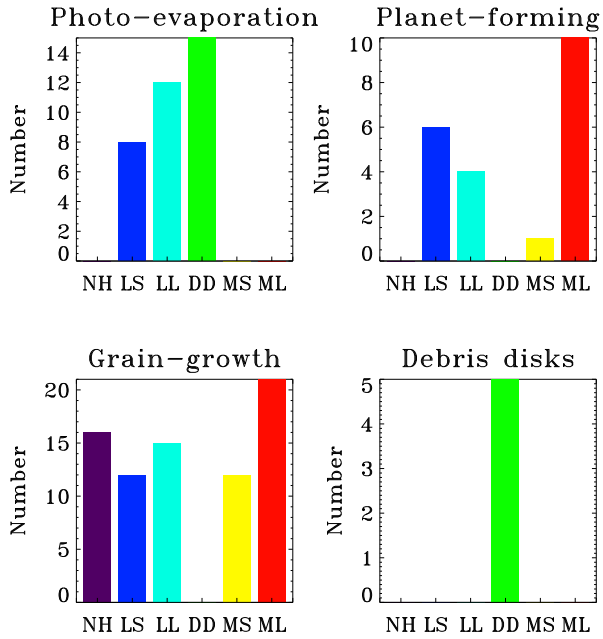

Figure 9.8: *Comparison of the categorization by the Cieza et al. studies with the classification of this study.*

9.5.6 Evolution

The $L_{\rm disk}/L_*$ ratio is generally taken as a measure of disk evolution. For the targets in this study, a clear trend is seen, with larger cavity radii and generally more non-accretors for lower $L_{\rm disk}/L_*$ (Figure 9.9a). This implies a general growth of cavity sizes with time.

A relation between disk mass and cavity radius has been noted in previous studies and interpreted as a gravitational process, where larger disk masses produce more massive planets, clearing larger cavities (Merín et al. 2010). This study shows no trend between disk mass and cavity size and generally more massive disks for accretors than for non-accretors (Figure 9.9b).

Both trends are susceptible due to the uncertainties in r_{cav} and could be biased due to the presence of many low-mass disks with large cavities in our sample, which are more likely to be debris disks than transition disks.

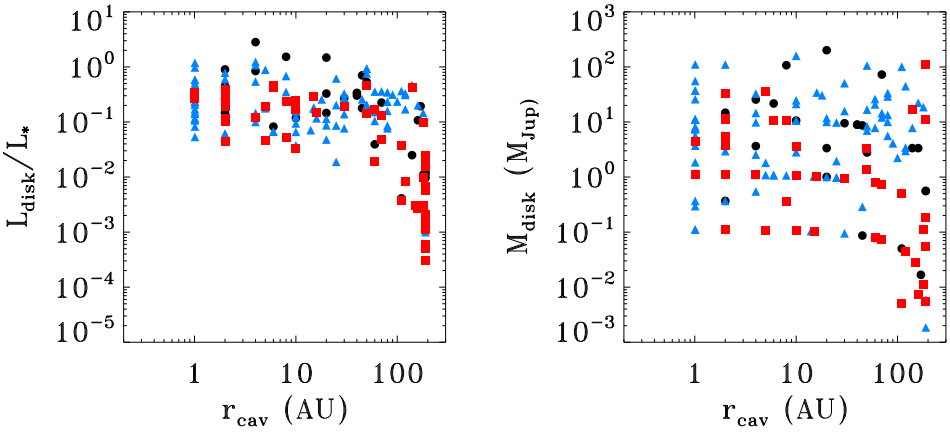

Figure 9.9: *The relation between cavity radius and L_{disk}/L_* and disk mass. Blue triangles indicate accretors, red squares non-accretors, black circles unknown.*

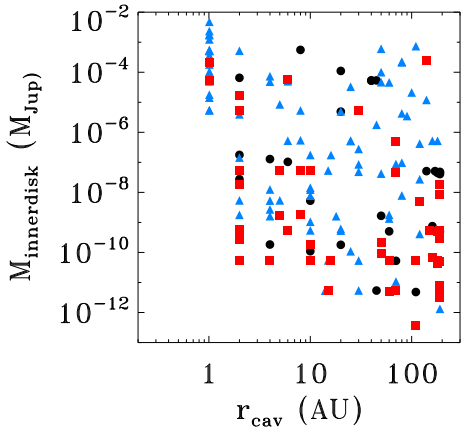

Figure 9.10: *The relation between cavity radius and inner disk mass. Blue triangles indicate accretors, red squares non-accretors, black circles unknown.*

9.5.7 Inner disk

Some transition disks are known to have an inner disk, while others have a completely empty cavity (e.g. Brown et al. 2007; Andrews et al. 2011). Some transition disk studies differentiate between these two types of disks as pre-transitional (with inner disk) and transitional disks (without inner disk), interpreting this as an evolutionary effect where the inner disk is expected to disappear with time due to accretion onto the star (Espaillat et al. 2014). However, with the measured accretion rates and inner disk masses the lifetime of the inner disk is very short (Owen et al. 2011), implying that for the inner disk to be detected it must be replenished continuously by the outer disk. Therefore, we do not distinguish between these two types of disks but use the $\delta_{\rm dust}$ value (a free parameter in our SED modeling) as a continuous parameter to fit the near infrared excess in the SEDs. Plotting the inner disk mass versus the cavity radius (Figure 9.10) reveals no significant trends (the disks with $r_{\rm cav}$=1 are disks without inner holes and there is no real inner disk) and the mass of the inner disk is spread over a large range for all cavity sizes. Accretors appear to have a slightly higher inner disk mass than non-accretors. This implies a possible division between transition disks with small cavities without inner disk and transition disks with large cavities with inner disk, each with their own origin.

9.5.8 Cavity radii and exoplanets

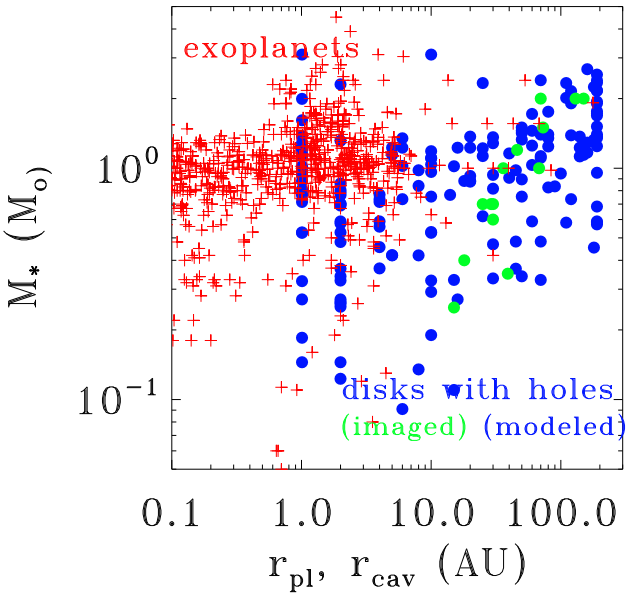

Figure 9.11: *Comparison of exoplanet orbital radii with transition disk cavity radii. Exoplanet orbital radii are indicated as red crosses, disk cavities with circles in blue (SED-modeling of this study) and green (millimeter imaging).*

If the origin of the dust cavity radii lies in forming planets, a correlation should exist between the orbital radii of exoplanets and disk cavity radii (Figure 9.11). Although both

samples are biased, a connection appears to exist, with the cavity radii several factors higher than the orbital radii. According to planet-disk interaction models, planet are expected to clear cavities up to twice their orbital radius (Pinilla et al. 2012a). A trend between cavity radius and stellar mass (blue and green points in Figure 9.11) as seen in previous work (M10) is seen as well.

9.6 Summary

The main results of this work are summarized as follows.

1. A large sample of ~200 transition disk candidates is presented and analyzed. Candidates are primarily selected from the *Spitzer* catalogs using the color criteria from Merín et al. (2010), with some additional targets from the literature.

2. The *Spitzer* data of the targets have been complemented with new submillimeter fluxes, *Herschel*-PACS archival data and optical/near infrared spectroscopy for spectral typing and accretion properties.

3. All targets are analyzed using RADMC-3D modeling with a limited number of parameters: disk mass, inner disk mass, scale height and flaring, and disk cavity radius, where the latter is the main parameter of interest.

4. The derived cavity sizes are consistent with imaging/modeling results in the literature.

5. Using the derived properties, the disks are categorized in disks without holes, large/small holes and massive/low-mass disks and very low scale height disks. The latter are likely debris disks. A large fraction of the targets falls in the category of disks with large holes, including several previously imaged disks.

6. Based on this classification, 133 targets (72% of the sample) are disks with cavities, including about 70 new transition disks that had not been identified before.

7. The color criteria are evaluated and compared for the targets in the Cieza studies (Cieza et al. 2010, 2012b; Romero et al. 2012). In general, our color criteria are a proper tool to select transition disk candidates.

8. The evolutionary parameter $L_{\rm disk}/L_*$ decreases with increasing cavity radius.

9. The cavity radius increases with stellar mass, suggesting a connection with exoplanet orbital radii.

10. The sample list provides a large number of transition disks that are suitable for follow-up observations with ALMA.

9.A Sample

Table 9.12: *Sample of transition disk candidates*

ID	Target	RA	Dec	Reg[a]	d[b] (pc)	Color[c]	Origin data	Prev.[d]	Ref
1	TCha	11 57 13.53	-79 21 31.5	ϵ Cha	108	[L]	Other	Imag.	1,2
2	RECX11	08 47 01.80	-78 59 35.2	η Cha	97	-	Other	TD	3,4
3	RECX5	08 42 27.09	-78 57 47.9	η Cha	97	[A]	Other	PF	5,4
4	CHXR22E	11 07 13.30	-77 43 49.9	ChaI	160	-	Other	TD	6,7
5	ISO52	11 04 42.58	-77 41 57.1	ChaI	160	[B]	GB	V	8
6	CSCha	11 02 25.11	-77 33 35.9	ChaI	160	[L]	c2d	V	8
7	11094742-7726290	11 09 47.27	-77 26 29.5	ChaI	160	[B]	GB		
9	T54	11 12 42.69	-77 22 23.1	ChaI	160	[L]	GB	CB	9
10	T21	11 06 15.41	-77 21 56.9	ChaI	160	-	Other	TD	6,7
11	SZCha	10 58 16.77	-77 17 17.1	ChaI	160	-	-	TD	9
12	T35	11 08 39.05	-77 16 04.2	ChaI	160	[A]	GB	TD/V	6,10
13	ISO-ChaII29	12 59 10.19	-77 12 13.7	ChaII	180	[L]	c2d		
14	T56	11 17 37.01	-77 04 38.1	ChaI	160	-	-	TD/V	6,10
15	CRCha	10 59 06.97	-77 01 40.3	ChaI	160	-	-	V	8
16	WWCha	11 10 00.11	-76 34 57.9	ChaI	160	[B]	-	V	8
17	11062554-7633418	11 06 25.47	-76 33 42.2	ChaI	160	[B]	GB		
18	T25	11 07 19.15	-76 03 04.9	ChaI	160	[A][L]	Other	V	11,7
20	MPMus	13 22 07.55	-69 38 12.2	Isol.	100	[B]	Other	TD	12,13
21	HD142527	15 56 41.89	-42 19 23.3	Isol.	140	-	-	Imag.	14
22	J16232807-4015368	16 23 28.09	-40 15 36.9	LupVI	150	[A][L]	GB		
23	Sz111	16 08 54.69	-39 37 43.1	LupIII	200	[A][L]	c2d	LU	15
24	Lup60	16 10 29.56	-39 22 14.7	LupIII	200	[A]	c2d	GG	16
25	J160830.3-390611	16 08 30.26	-39 06 11.1	LupIII	200	[B]	c2d	L	15
26	Sz104	16 08 30.80	-39 05 48.8	LupIII	200	[B]	c2d	H	15
27	Sz91	16 07 11.60	-39 03 47.7	LupIII	200	[L]	c2d	PF	16
28	J160855.5-390234	16 08 55.52	-39 02 33.9	LupIII	200	[A]	c2d	L/PE	17,18
29	Sz84	15 58 02.50	-37 36 02.8	LupI	150	[L] *	c2d	TD	19
30	16182186-3730298	16 18 21.88	-37 30 29.9	LupV	150	[L]	GB		
31	16225309-3724373	16 22 53.10	-37 24 37.4	LupV	150	[L]	GB		
32	J19002346-3712242	19 00 23.47	-37 12 24.2	CrA	150	[A]	GB		
33	HD135344	15 15 48.44	-37 09 16.0	Isol.	140	[B]	-	Imag.	20
34	CrA-466	19 01 18.95	-36 58 28.3	CrA	150	-	Other	TD	21
35	Sz76	15 49 30.80	-35 49 52.0	LupI	150	[B]	Other		22

Refs. 1) Wahhaj et al. (2010), 2) Huélamo et al. (2015), 3) Megeath et al. (2005), 4) Sicilia-Aguilar et al. (2009), 5) Bouwman et al. (2010), 6) Kim et al. (2009), 7) Luhman et al. (2008), 8) Espaillat et al. (2011), 9) Kim et al. (2009), 10) Espaillat et al. (2011), 11) Espaillat et al. (2011), 12) Cortes et al. (2009), 13) Silverstone et al. (2006), 14) Ohashi (2008), 15) Merín et al. (2008), 16) Romero et al. (2012), 17) Merín et al. (2008), 18) Romero et al. (2012), 19) Merín et al. (2010), 20) Brown et al. (2009), 21) Sicilia-Aguilar et al. (2008), 22) Padgett et al. (2006), 23) Andrews et al. (2011), 24) Rosenfeld et al. (2013), 25) Cieza et al. (2010), 26) Andrews et al. (2010), 27) van der Marel et al. (2013), 28) van Kempen et al. (2009), 29) Andrews et al. (2009), 30) McClure et al. (2010), 31) Mathews et al. (2012), 32) Harvey et al. (2007), 33) Furlan et al. (2011), 34) Andrews et al. (2011), 35) Wahhaj et al. (2010), 36) Rebull et al. (2010), 37) Cieza et al. (2012b), 38) Isella et al. (2010b), 39) Monnier et al. (2008), 40) Cieza et al. (2012b), 41) Furlan et al. (2011), 42) Isella et al. (2010a), 43) Furlan et al. (2011), 44) Piétu et al. (2005), 45) Najita et al. (2010), 46) Piétu et al. (2006), 47) Ireland & Kraus (2008), 48) Hughes et al. (2009), 49) Carpenter et al. (2008), 50) Cieza et al. (2012a)

Notes. [a] Full names of the regions: Cha = Chamaeleon, Lup = Lupus, CrA = Corona Australis, Oph = Ophiuchus, UppS = Upper Sco, Oph = Ophiuchus, Tau = Taurus, Aur = Auriga, Per = Perseus, TWH = TW Hydrae, Isol. = Isolated. [b] Distances were adopted from the literature as follows: 120 pc for Oph (Loinard et al. 2008); 150 pc for Lup I, IV, V and VI and 200 pc for LupIII (Comerón 2008; Comerón et al. 2009); 250 pc for Per (Jørgensen et al. 2006); 140 pc for Tau (Kenyon et al. 2008); 450 pc for Aur (Broekhoven-Fiene et al. 2014); 145 pc for Upp Sco (Carpenter et al. 2008); 150 pc for Corona Australis (Sicilia-Aguilar et al. 2008); 109 pc for ϵ Cha(Torres et al. 2008); 160 pc for ChaI (Kim et al. 2009); 180 pc for ChaII (Alcalá et al. 2008); 97 pc for η Cha(Mamajek et al. 1999); and 430 pc for Ser (Dzib et al. 2010). [c] An asterix (*) indicates this target was part of the M10 sample. [d] The full explanation previous classifications is as follows, according to their recording papers. 1) Cieza et al. (2010): "PF"=Planet-forming disk, "GG"=Grain-growth dominated disk, "PE"=Photoevaportive disk. 2) Merín et al. (2008); Harvey et al. (2007): "L"=low infrared excess or anemic disk, "H"=high infrared excess, "T"=T Tauri-like infrared excess. 3) Others: "PTD" = pre-transitional disk, "V" = sea-saw variability.

Table 9.12: *Sample of transition disk candidates*

ID	Target	RA	Dec	Reg[a]	d[b] (pc)	Color[c]	Origin data	Prev.[d]	Ref
36	J154508.9-341734	15 45 08.88	-34 17 33.7	LupI	150	-	Other	LU	15
38	RXJ1615.3-3255	16 15 20.23	-32 55 04.9	Lup	185	[B] *	c2d	Imag.	23
39	V4046Sgr	18 14 10.47	-32 47 34.5	Isol.	73	-	-	Imag.	24
40	J163154.7-250324	16 31 54.73	-25 03 24.0	Oph	125	[B]	c2d	GG	25
41	J163205.5-250236	16 32 05.52	-25 02 36.2	Oph	125	[A]	c2d	PF	25
43	J163023.4-245416	16 30 23.39	-24 54 16.1	Oph	125	[B]	c2d		
44	WSB63	16 28 54.06	-24 47 44.3	Oph	125	[A]	c2d	PF	25
45	SR24S	16 26 58.51	-24 45 37.0	Oph	125	-	c2d	Imag.	26
46	RXJ1633.9-2442	16 33 55.60	-24 42 05.0	Oph	125	[A]	c2d	Imag.	25,50
47	ISO-Oph43	16 26 27.53	-24 41 53.6	Oph	125	[B]	c2d		
48	WSB60	16 28 16.51	-24 36 58.3	Oph	125	[B]	c2d	Imag.	23
49	J163115.7-243402	16 31 15.74	-24 34 02.0	Oph	125	[B]	c2d	GG	25
50	J162245.4-243124	16 22 45.39	-24 31 23.8	Oph	125	[A] *	c2d	PE	25
51	IRS48	16 27 37.19	-24 30 34.8	Oph	125	-	Other	Imag.	27,28
52	DoAr44	16 31 33.46	-24 27 37.4	Oph	125	[B]	c2d	Imag.	29
53	J162435.2-242620	16 24 35.20	-24 26 20.0	Oph	125	[A]	c2d		
54	SR21	16 27 10.28	-24 19 12.5	Oph	125	-	-	Imag.	20
55	J162309.2-241705	16 23 09.22	-24 17 04.6	Oph	125	[A]	c2d	PTD	30
56	J163136.8-240420	16 31 36.77	-24 04 19.8	Oph	125	[L]	c2d		
58	J162648.6-235634	16 26 48.64	-23 56 34.1	Oph	125	[B]	c2d		
59	J162802.6-235504	16 28 02.60	-23 55 04.0	Oph	125	[A]	c2d	PE	25
60	oph62	16 25 06.92	-23 50 50.4	Oph	125	[A] *	c2d	PF	25
61	J162532.5-232626	16 25 32.50	-23 26 26.0	Oph	125	[A]	c2d		
62	J162218.5-232148	16 22 18.52	-23 21 48.1	Oph	125	[B]	c2d	GG	25
63	DoAr28	16 26 47.42	-23 14 52.2	Oph	125	-	HREL	TD	30
64	J160421.7-213028	16 04 21.70	-21 30 28.4	UppS	145	[L]	-	Imag.	31
65	18015423-0437531	18 01 54.24	-04 37 53.1	Ser	415	[L]	GB		
66	18044921-0436413	18 04 49.20	-04 36 41.5	Ser	415	[B]	GB		
67	18270980-0414297	18 27 09.79	-04 14 29.8	Ser	415	[L]	GB		
68	18272873-0406248	18 27 28.73	-04 06 24.8	Ser	415	[L]	GB		
69	18273408-0403247	18 27 34.08	-04 03 24.8	Ser	415	[L]	GB		
70	18273858-0402289	18 27 38.57	-04 02 28.9	Ser	415	[A][L]	GB		
71	18255765-0357040	18 25 57.66	-03 57 04.0	Ser	415	[L]	GB		
73	18291383-0342355	18 29 13.84	-03 42 35.5	Ser	415	[L]	GB		
74	18284156-0341507	18 28 41.56	-03 41 50.7	Ser	415	[L]	GB		
75	18283439-0339371	18 28 34.40	-03 39 37.2	Ser	415	[L]	GB		
76	18272161-0314158	18 27 21.62	-03 14 15.9	Ser	415	[L]	GB		
77	18222604-0304383	18 22 26.04	-03 04 38.3	Ser	415	[L]	GB		
78	18330328-0244021	18 33 03.30	-02 44 02.2	Ser	415	[B]	GB		
79	18324685-0243273	18 32 46.86	-02 43 27.4	Ser	415	[L]	GB		
80	18304127-0242335	18 30 41.26	-02 42 33.7	Ser	415	[L]	GB		
81	18324783-0239401	18 32 47.83	-02 39 40.1	Ser	415	[B]	GB		
82	J18321275-0222377	18 32 12.75	-02 22 37.8	Ser	415	[A][L]	GB		
83	18292883-0221157	18 29 28.84	-02 21 15.7	Ser	415	[A][L]	GB		
84	18291450-0220575	18 29 14.50	-02 20 57.5	Ser	415	[L]	GB		
85	18304121-0220189	18 30 41.20	-02 20 19.1	Ser	415	[B]	GB		
86	J18314556-0218408	18 31 45.57	-02 18 40.9	Ser	415	[A]	GB		
88	18311986-0208161	18 31 19.86	-02 08 16.1	Ser	415	[A]	GB		
89	18323005-0204130	18 32 30.06	-02 04 13.0	Ser	415	[A][L]	GB		
90	18292804-0204042	18 29 28.07	-02 04 04.7	Ser	415	[A]	GB		
91	18293961-0202414	18 29 39.60	-02 02 41.4	Ser	415	[B]	GB		
92	J18303289-0200514	18 30 32.89	-02 00 51.3	Ser	415	[A][L]	GB		
93	18311732-0200461	18 31 17.32	-02 00 46.1	Ser	415	[A]	GB		
94	18312875-0159125	18 31 28.75	-01 59 12.5	Ser	415	[A]	GB		
95	18315497-0157330	18 31 54.98	-01 57 33.1	Ser	415	[L]	GB		
96	18313657-0157320	18 31 36.57	-01 57 32.0	Ser	415	[A]	GB		

Table 9.12: *Sample of transition disk candidates*

ID	Target	RA	Dec	Reg[a]	d[b] (pc)	Color[c]	Origin data	Prev.[d]	Ref
97	18313343-0155182	18 31 33.43	-01 55 18.2	Ser	415	[A]	GB		
98	18315077-0153393	18 31 50.77	-01 53 39.3	Ser	415	[B]	GB		
99	J18303321-0152563	18 30 33.22	-01 52 56.2	Ser	415	[A][L]	GB		
100	18295741-0151541	18 29 57.41	-01 51 54.1	Ser	415	[A][L]	GB		
101	18294721-0148301	18 29 47.21	-01 48 30.2	Ser	415	[A][L]	GB		
102	18293368-0145103	18 29 33.69	-01 45 10.3	Ser	415	[B]	GB		
103	18290819-0139215	18 29 08.19	-01 39 21.5	Ser	415	[B]	GB		
104	18314110-0128035	18 31 41.10	-01 28 03.6	Ser	415	[L]	GB		
105	18290391-0115357	18 29 03.92	-01 15 35.8	Ser	415	[L]	GB		
106	18371575-0026561	18 37 15.75	-00 26 56.1	Ser	415	[L]	GB		
107	18381010-0023452	18 38 10.10	-00 23 45.2	Ser	415	[L]	GB		
108	18371444-0023261	18 37 14.45	-00 23 26.2	Ser	415	[L]	GB		
110	18385989-0008097	18 38 59.90	-00 08 09.9	Ser	415	[L]	GB		
111	J182813.5+000-249	18 28 13.51	-00 02 49.1	Ser	415	[B]	c2d	TT	32
112	J182821.6+000016	18 28 21.58	+00 00 16.4	Ser	415	[B]	c2d	L	32
113	18384257+0001324	18 38 42.59	+00 01 32.5	Ser	415	[A][L]	GB		
114	18392594+0006382	18 39 25.96	+00 06 38.4	Ser	415	[A]	GB		
115	J182850.2+000950	18 28 50.21	+00 09 49.7	Ser	415	[B]	c2d	F	32
116	183549.4+001002	18 35 49.38	+00 10 01.7	Ser	415	[L]	GB		
117	18385571+0014431	18 38 55.72	+00 14 43.1	Ser	415	[A][L]	GB		
118	18394048+0014497	18 39 40.50	+00 14 49.7	Ser	415	[B]	GB		
119	18374209+0016519	18 37 42.09	+00 16 52.0	Ser	415	[L]	GB		
120	J182911.5+002039	18 29 11.49	+00 20 38.8	Ser	415	[A] *	c2d		
121	18375663-0023253	18 37 56.63	-00 23 25.3	Ser	415	[A]	GB		
122	18381580+0024218	18 38 15.81	+00 24 21.9	Ser	415	[L]	GB		
123	J18295130+0027477	18 29 51.30	+00 27 47.9	Ser	415	[L]	c2d	LU	32
124	serp22	18 28 29.06	+00 27 56.0	Ser	415	[A] *	c2d		
125	18401205+0029276	18 40 12.06	+00 29 27.7	Ser	415	[B]	GB		
126	J182901.2+002933	18 29 01.22	+00 29 33.0	Ser	415	[B]	c2d	L	32
127	Serp127	18 29 44.10	+00 33 56.0	Ser	415	[A][L] *	c2d	LU	32
128	J182935.6+003504	18 29 35.62	+00 35 03.9	Ser	415	[A] *	c2d	LU	32
129	18381447+0035099	18 38 14.48	+00 35 09.8	Ser	415	[L]	GB		
130	18401486+0037042	18 40 14.88	+00 37 04.2	Ser	415	[A][L]	GB		
131	Serp111	18 29 36.19	+00 42 16.7	Ser	415	[A] *	c2d	LU	32
132	J182955.3+004939	18 29 55.32	+00 49 39.3	Ser	415	[A]	c2d	TT	32
133	J183008.6+005847	18 30 08.62	+00 58 46.7	Ser	415	[B]	c2d	TT	32
134	RXJ0432.8+1735	04 32 53.24	+17 35 33.7	Tau	140	-	Tau	TD	33
135	DMTau	04 33 48.73	+18 10 10.0	Tau	140	-	Tau	Imag./V	34,10
136	UXTauA	04 30 04.00	+18 13 49.3	Tau	140	[A]	Other	Imag.	34,35
137	043339.0+222720	04 33 39.00	+22 27 20.0	Tau	140	[A]	Tau		33
138	043326.2+224529	04 33 26.20	+22 45 29.0	Tau	140	[L]	Tau		36
139	J04390525+2337450	04 39 05.25	+23 37 45.0	Tau	140	[B]	GB	PTD	33
140	043649.1+241258	04 36 49.10	+24 12 58.0	Tau	140	[L]	Tau	DD	37
142	MWC758	05 30 27.53	+25 19 56.9	Isol.	200	-	Tau	Imag.	38
144	044555.7+261858	04 45 55.70	+26 18 58.0	Tau	140	[L]	Tau		
145	DHTauAB	04 29 41.50	+26 32 58.0	Tau	140	[A]	Tau		
146	043044.7+263308	04 30 44.70	+26 33 08.0	Tau	140	[L]	Tau		
147	J04214631+2659296	04 21 46.32	+26 59 29.6	Tau	140	[A]	Tau		
148	IPTau	04 24 57.08	+27 11 56.5	Tau	140	-	Tau	V	8
149	V892Tau	04 18 40.62	+28 19 15.5	Tau	140	-	Tau	CB-disk	39
150	V410X-ray6	04 19 01.10	+28 19 42.0	Tau	140	[A]	Tau	PF/TD	40,41
151	042254.6+282354	04 22 54.60	+28 23 54.0	Tau	140	[L]	Tau		
152	V819Tau	04 19 26.26	+28 26 14.3	Tau	140	-	Tau	TD	33
153	RYTau	04 21 57.41	+28 26 35.6	Tau	140	-	Tau	Imag./V	42,10
154	V410X-ray2	04 18 34.40	+28 30 30.0	Tau	140	[A]	Tau	TD	33

Table 9.12: *Sample of transition disk candidates*

ID	Target	RA	Dec	Reg[a]	d[b] (pc)	Color[c]	Origin data	Prev.[d]	Ref
155	041542.7+290959	04 15 42.78	+29 09 59.0	Tau	140	[A][L]	Tau	TD	33
156	041332.3+291726	04 13 32.30	+29 17 26.0	Tau	140	[A]	Tau		
157	J032800.1+300847	03 28 00.09	+30 08 47.0	Per	250	[B]	c2d		
158	LkCa19	04 55 36.96	+30 17 55.2	Tau	140	-	Other	TD	43,35
159	ABAur	04 55 45.85	+30 33 04.3	Tau	140	-	-	Imag.	44
160	J033341.3+311341	03 33 41.29	+31 13 41.0	Per	250	[B]	c2d		
161	ASR118	03 28 56.97	+31 16 22.3	Per	250	[B] *	c2d		
162	MBO22	03 29 29.27	+31 18 34.7	Per	250	[A] *	c2d	PF	25
163	J032856.6+311836	03 28 56.65	+31 18 35.5	Per	250	[B]	c2d		
164	J034219.3+314327	03 42 19.27	+31 43 27.0	Per	250	[B]	c2d		
165	J034227.1+314433	03 42 27.12	+31 44 32.9	Per	250	[A] *	c2d		
166	J034109.1+314438	03 41 09.13	+31 44 37.9	Per	250	[B]	c2d		
167	J034355.2+315532	03 43 55.20	+31 55 32.0	Per	250	[A]	c2d		
168	J034434.8+315655	03 44 34.81	+31 56 55.2	Per	250	[A] *	c2d		
169	IC348LRL190	03 44 29.23	+32 01 15.7	Per	250	[A] *	c2d		
171	J034520.5+320634	03 45 20.46	+32 06 34.5	Per	250	[B]	c2d		
172	IC348-67	03 43 44.63	+32 08 17.8	Per	250	[A]	c2d	PF	37
173	LkH-alpha330	03 45 48.29	+32 24 11.8	Per	250	[B]	c2d	Imag.	20
174	J04300424+3522238	04 30 04.25	+35 22 23.8	Aur	450	[A][L]	GB	PF	37
175	J04303235+3536133	04 30 32.35	+35 36 13.4	Tau	140	[L]	GB	PF	37
176	04300980+3540355	04 30 09.80	+35 40 35.6	Tau	140	[B]	GB		
177	J04304004+3542101	04 30 40.05	+35 42 10.3	Tau	140	[L]	GB	GG	37
178	J04303831+3549591	04 30 38.27	+35 49 59.3	Aur	450	[L]	GB		
179	J160044.5-415531	16 00 44.53	-41 55 31.2	LupIV	150	[B]	c2d	PF	16
180	J190058.1-364505	19 00 58.05	-36 45 05.0	UppS	145	[A]	GB	PF	16
181	03445614+3209152	03 44 56.14	+32 09 15.1	Per	250	[A]	c2d	PF	37
182	03442156+3215098	03 44 21.58	+32 15 09.7	Per	250	[A]	c2d	PE	37
183	03442257+3201536	03 44 22.58	+32 01 53.8	Per	250	[A]	c2d	PE	37
184	04330422+2921499	04 33 04.22	+29 21 50.0	Per	250	[A]	Tau	DD	37
185	J160825.76-390601.1	16 08 25.76	-39 06 01.1	LupIII	200	[B]	c2d	TT	15
186	RXJ1556.1-3655	15 56 02.10	-36 55 28.2	LupIII	150	[B]	Other		22
187	043150.5+242418	04 31 50.50	+24 24 18.0	Tau	140	[B]	Tau		
188	041413.5+281249	04 14 13.50	+28 12 49.0	Tau	140	[B]	Tau		
189	041841.3+282725	04 18 41.30	+28 27 25.0	Tau	140	[B]	Tau		
190	042025.5+270035	04 20 25.50	+27 00 35.0	Tau	140	[B]	Tau		
191	042921.6+270125	04 29 21.60	+27 01 25.0	Tau	140	[B]	Tau		
192	043249.1+225302	04 32 49.10	+22 53 02.0	Tau	140	[B]	Tau		
193	044221.0+252034	04 42 21.00	+25 20 34.0	Tau	140	[B]	Tau		
194	041539.1+281858	04 15 39.10	+28 18 58.0	Tau	140	[B]	Tau		
195	042318.2+264115	04 23 18.20	+26 41 15.0	Tau	140	[B]	Tau		
196	041414.5+282758	04 14 14.50	+28 27 58.0	Tau	140	[B]	Tau		
197	041915.8+290626	04 19 15.80	+29 06 26.0	Tau	140	[B]	Tau		
198	042155.6+275506	04 21 55.60	+27 55 06.0	Tau	140	[B]	Tau		
200	J160710.08-391103.5	16 07 10.08	-39 11 03.5	LupIII	200	[B]	c2d	L	15
201	J032741.47+302016.8	03 27 41.47	+30 20 16.8	Per	250	[B]	c2d		
202	J034345.17+320358.6	03 43 45.17	+32 03 58.6	Per	250	[A]	c2d		
203	J182815.26-000243.3	18 28 15.26	-00 02 43.3	Ser	415	[B]	c2d		
204	J162715.89-243843.2	16 27 15.89	-24 38 43.2	Oph	125	[B]	c2d		30
301	J130455.7-773949	13 04 55.74	-77 39 49.5	ChaII	180	[B] *	c2d		
303	J160115.5-415235	16 01 15.55	-41 52 35.3	LupIV	150	[B]	c2d	F	15
307	16083070-3828268	16 08 30.70	-38 28 26.8	LupIII	200	[B]	HREL	L	15
309	TWHya	11 01 51.91	-34 42 17.0	TWH	50	-	-	TD	45
310	15395742-3414567	15 39 57.42	-34 14 56.7	LupI	150	-	HREL		
314	16281385-2456113	16 28 13.85	-24 56 11.3	Oph	125	[B]	HREL		
316	16271587-2438433	16 27 15.87	-24 38 43.3	Oph	125	[B]	HREL		
317	16312019-2430009	16 31 20.19	-24 38 43.3	Oph	125	[B]	HREL		

Table 9.12: *Sample of transition disk candidates*

ID	Target	RA	Dec	Reg[a]	d[b] (pc)	Color[c]	Origin data	Prev.[d]	Ref
318	DoAr21	16 26 03.03	-24 23 36.4	Oph	125	[A] *	c2d		
319	J162740.3-242204	16 27 40.27	-24 22 04.0	Oph	125	[A]	c2d	CB	25
321	Serp48	18 28 58.08	+00 17 24.5	Ser	415	[LL] *	c2d		
322	18302986+0035004	18 30 29.86	+00 35 00.4	Ser	415	[B]	HREL		
325	LkCa15	04 39 17.78	+22 21 03.5	Tau	140	[A]	Tau	Imag./V	46,10
326	CoKu-Tau-4	04 41 16.79	+28 40 00.5	Tau	140	-	-	CB-disk	47
329	GMAur	04 55 10.98	+30 21 59.4	Tau	140	[A]	-	Imag./V	48,10
333	03370363+3039291	03 37 03.63	+30 39 29.1	Per	250	-	HREL		
334	03401579+3055047	03 40 15.79	+30 55 47.0	Per	250	[B]	HREL		
335	J033234.0+310056	03 32 34.00	+31 00 56.0	Per	250	[B] *	c2d		
348	UScoJ155837.1-225724	15 58 36.91	-22 57 15.3	UppS	145	[B]	Other		49
349	RXJ1842.9-3532	18 42 57.95	-35 32 42.7	UppS	145	[A]	Other		49
350	RXJ1852.3-3700	18 52 17.30	-37 00 11.9	UppS	145	[A]	Other		49

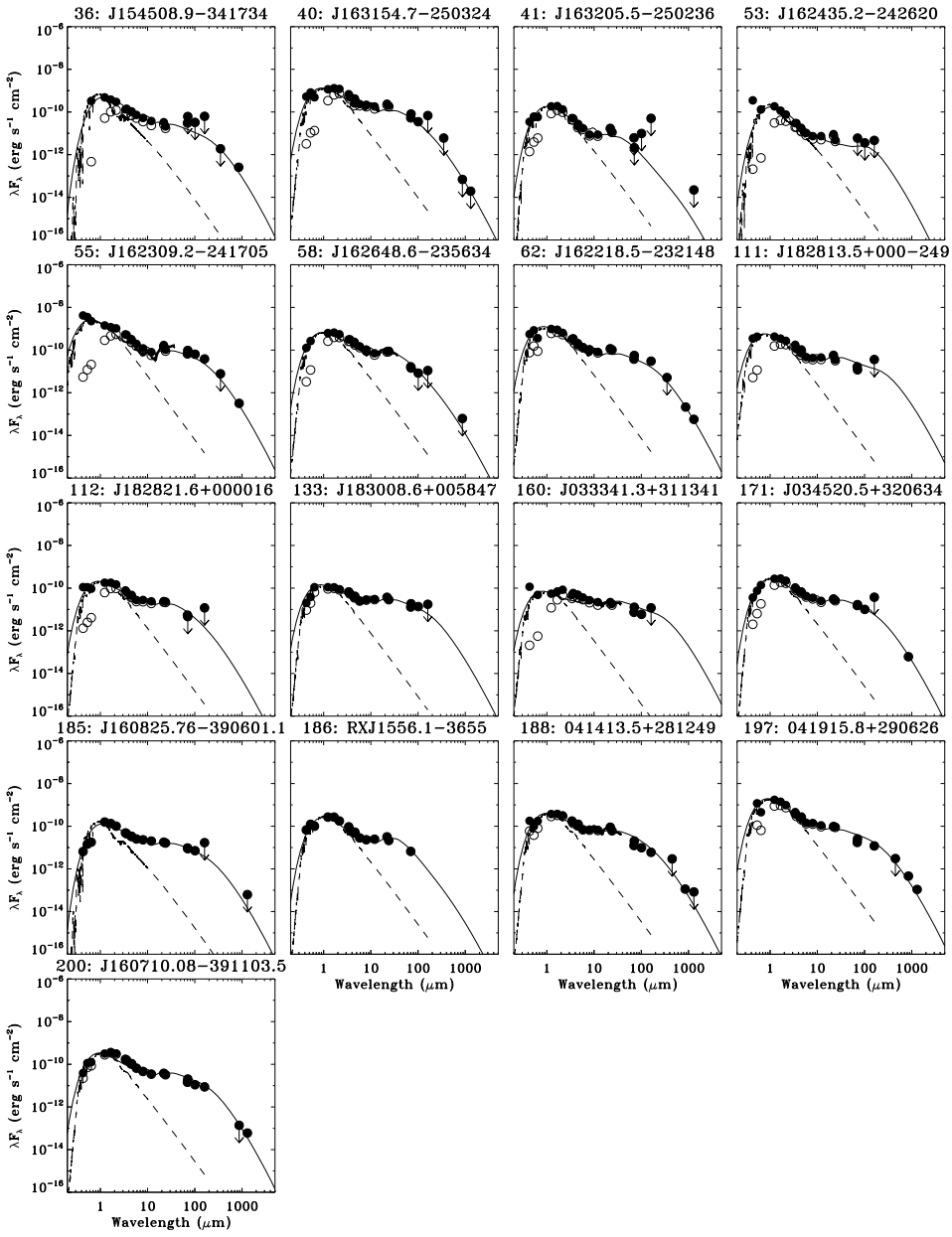

Figure 9.12: *SEDs of disks without holes. In this and subsequent Figures the dashed line indicates the stellar spectrum. Open circles denote observed fluxes before extinction correction, filled circles after extinction correction.*

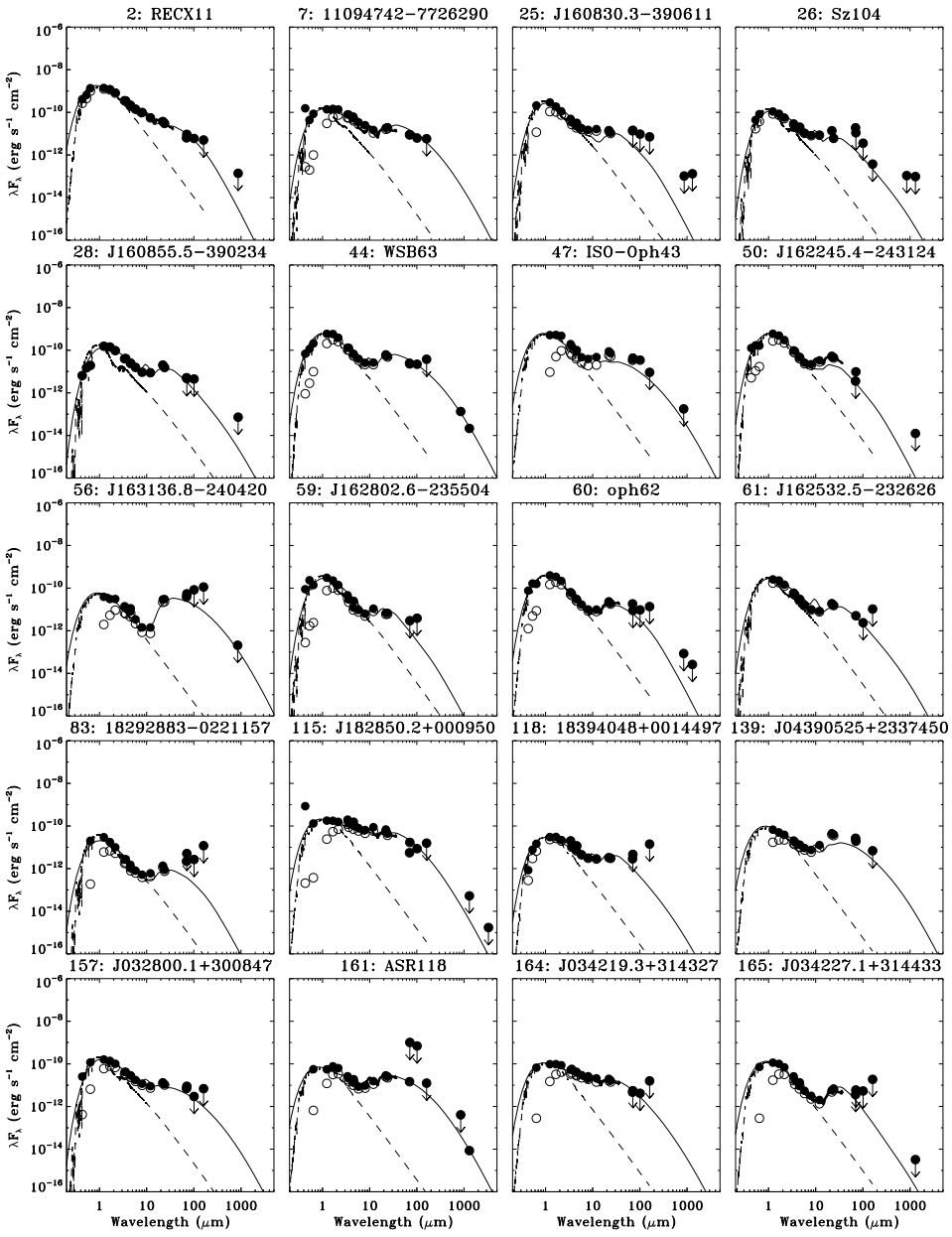

Figure 9.13: *SEDs of low-mass disks with small holes.*

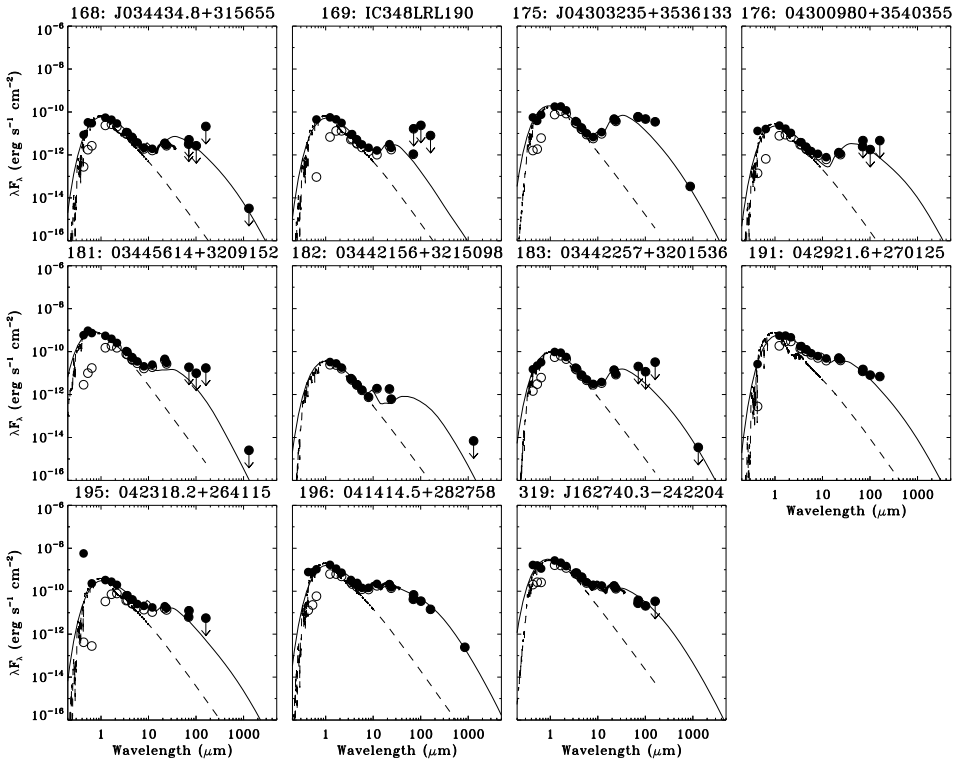

Figure 9.13: *SEDs of low-mass disks with small holes.*

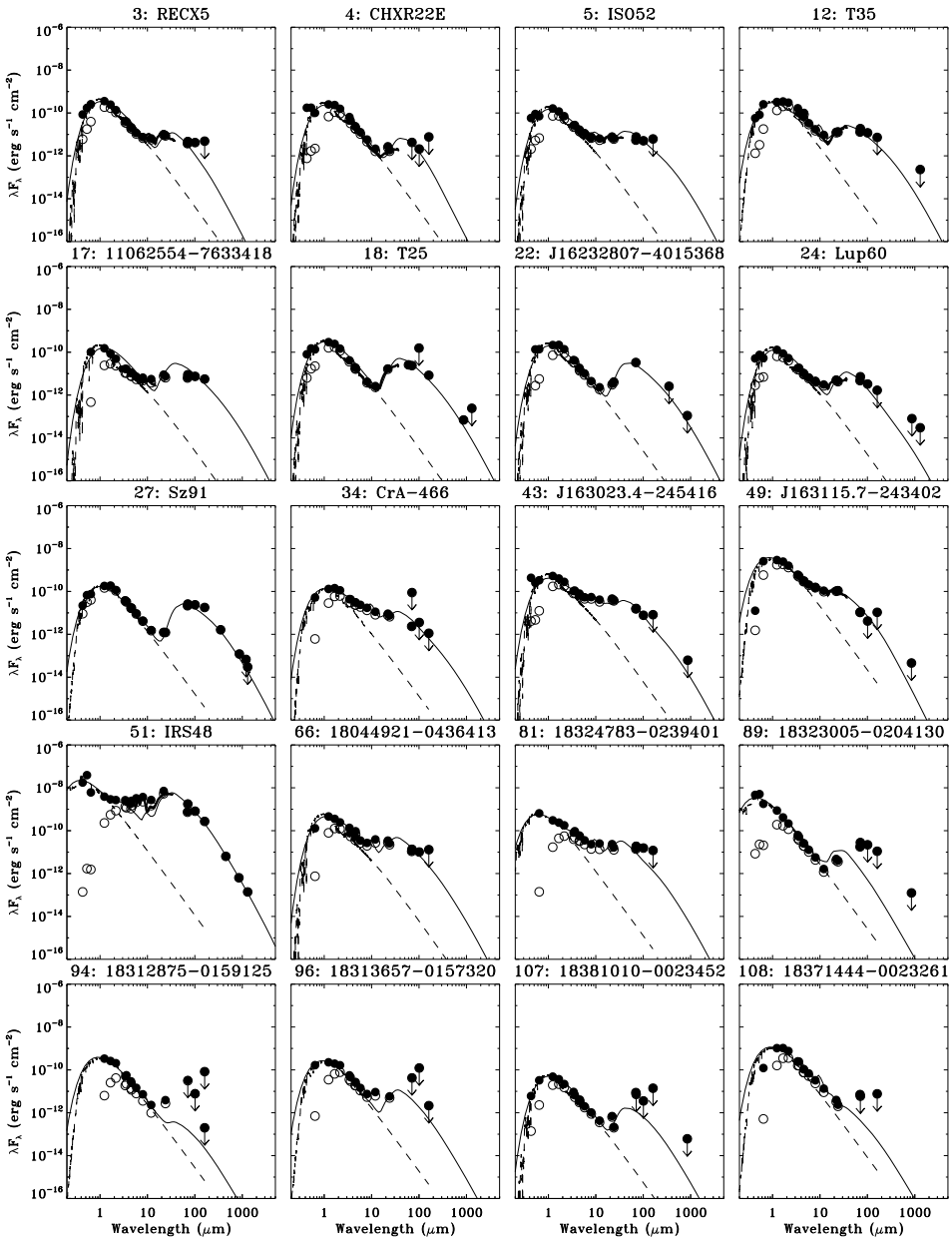

Figure 9.14: *SEDs of low-mass disks with large holes.*

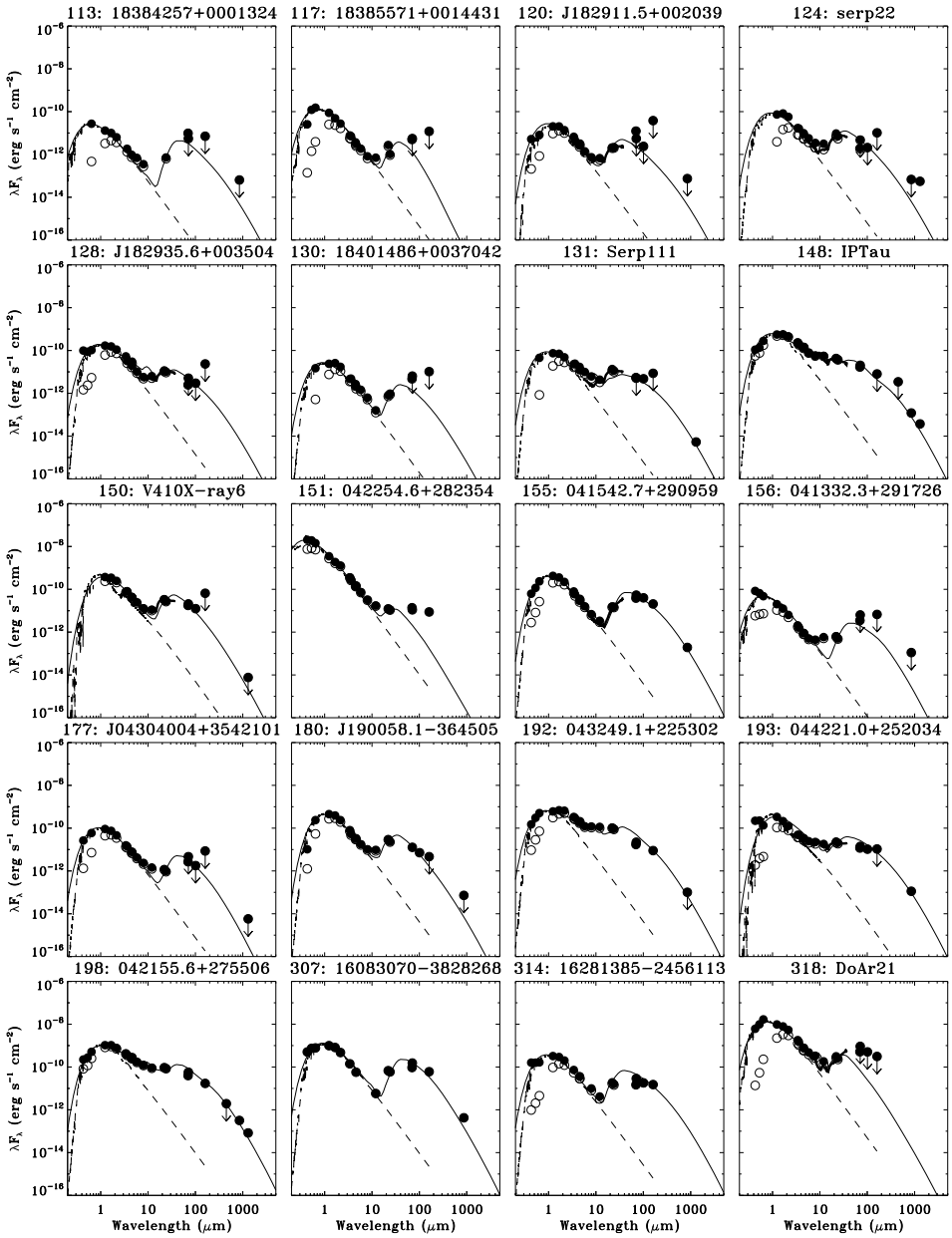

Figure 9.14: *SEDs of low-mass disks with large holes.*

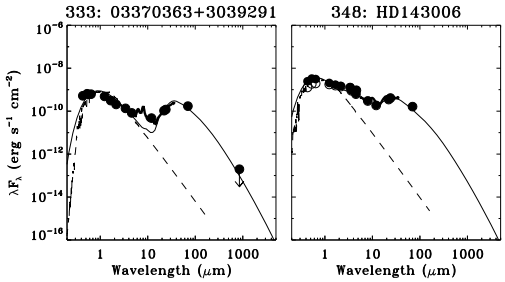

Figure 9.14: *SEDs of low-mass disks with large holes.*

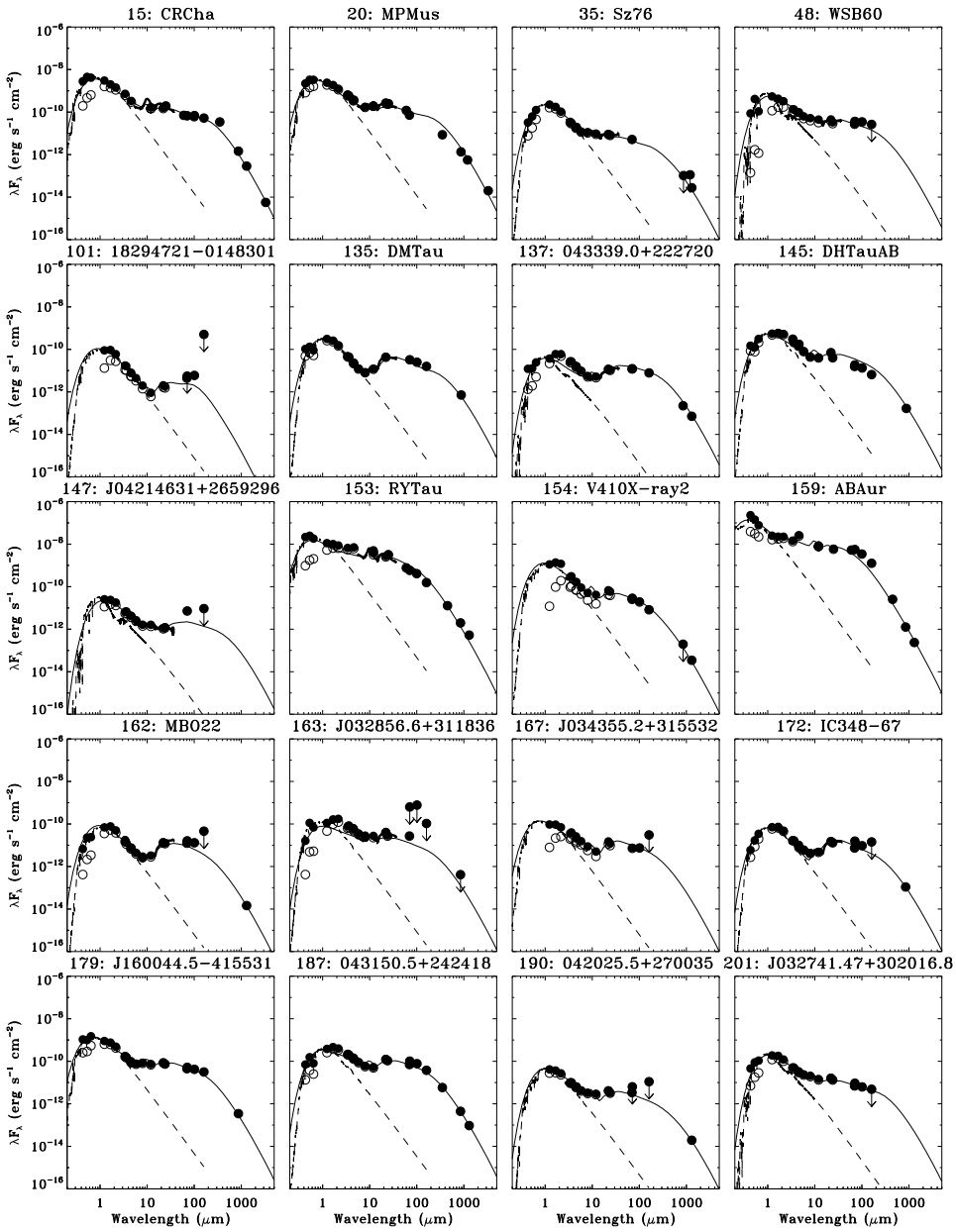

Figure 9.15: *SEDs of massive disks with small holes.*

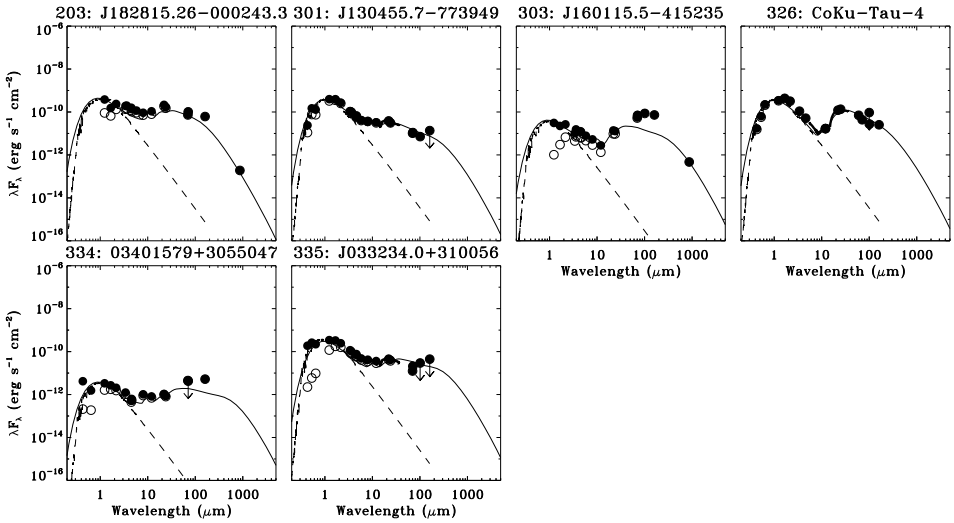

Figure 9.15: *SEDs of massive disks with small holes.*

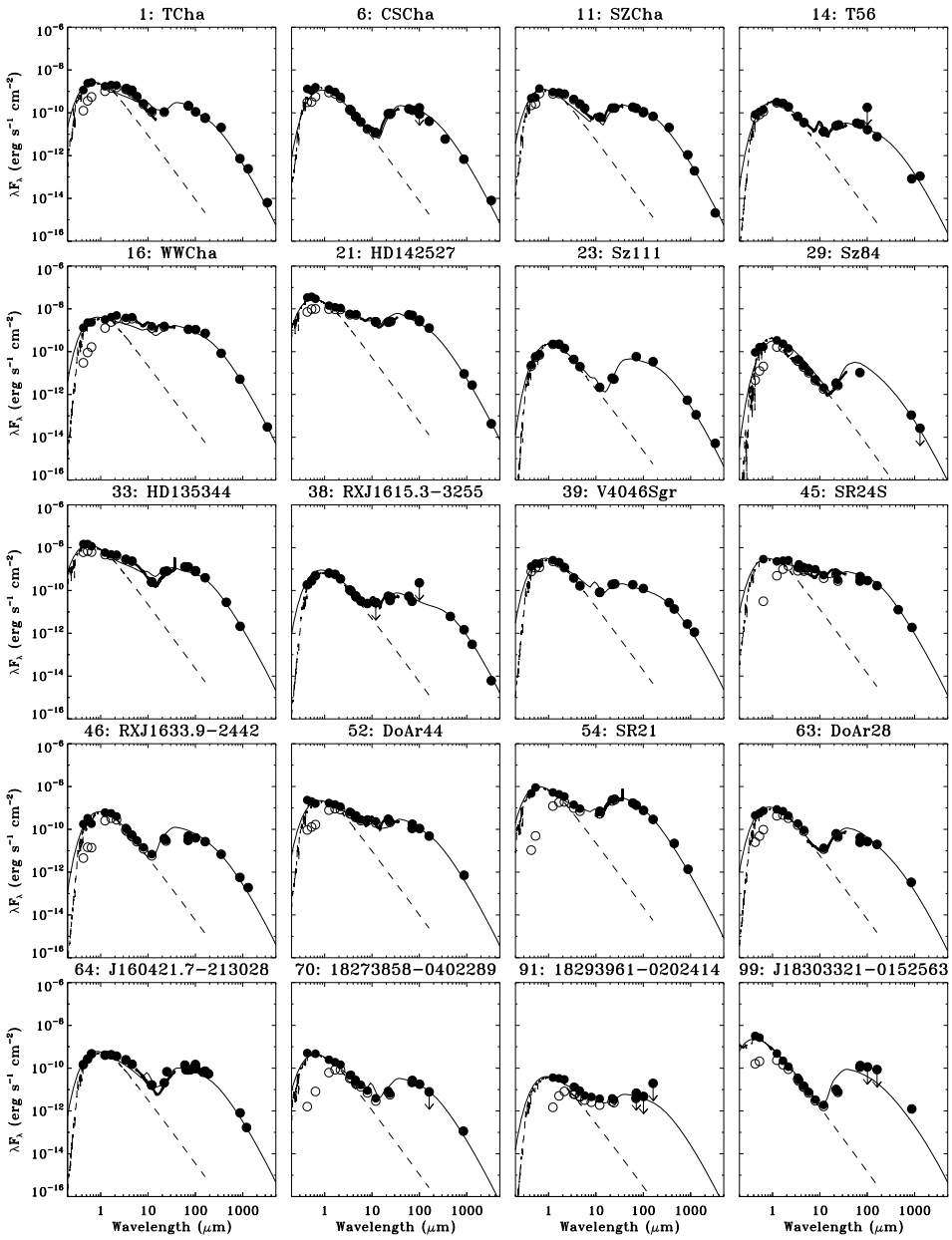

Figure 9.16: *SEDs of massive disks with large holes.*

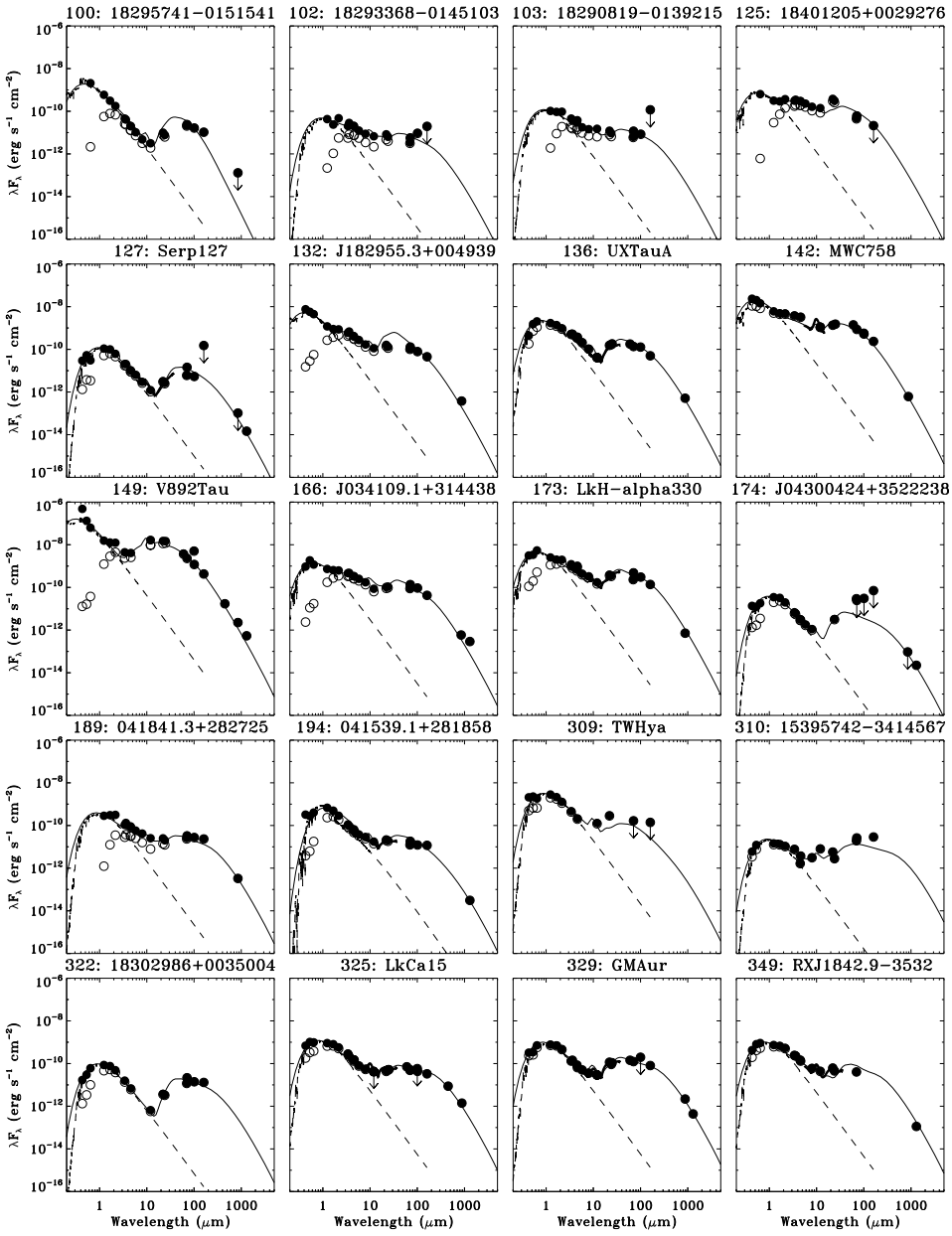

Figure 9.16: *SEDs of massive disks with large holes.*

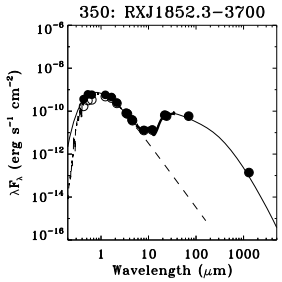

Figure 9.16: *SEDs of massive disks with large holes.*

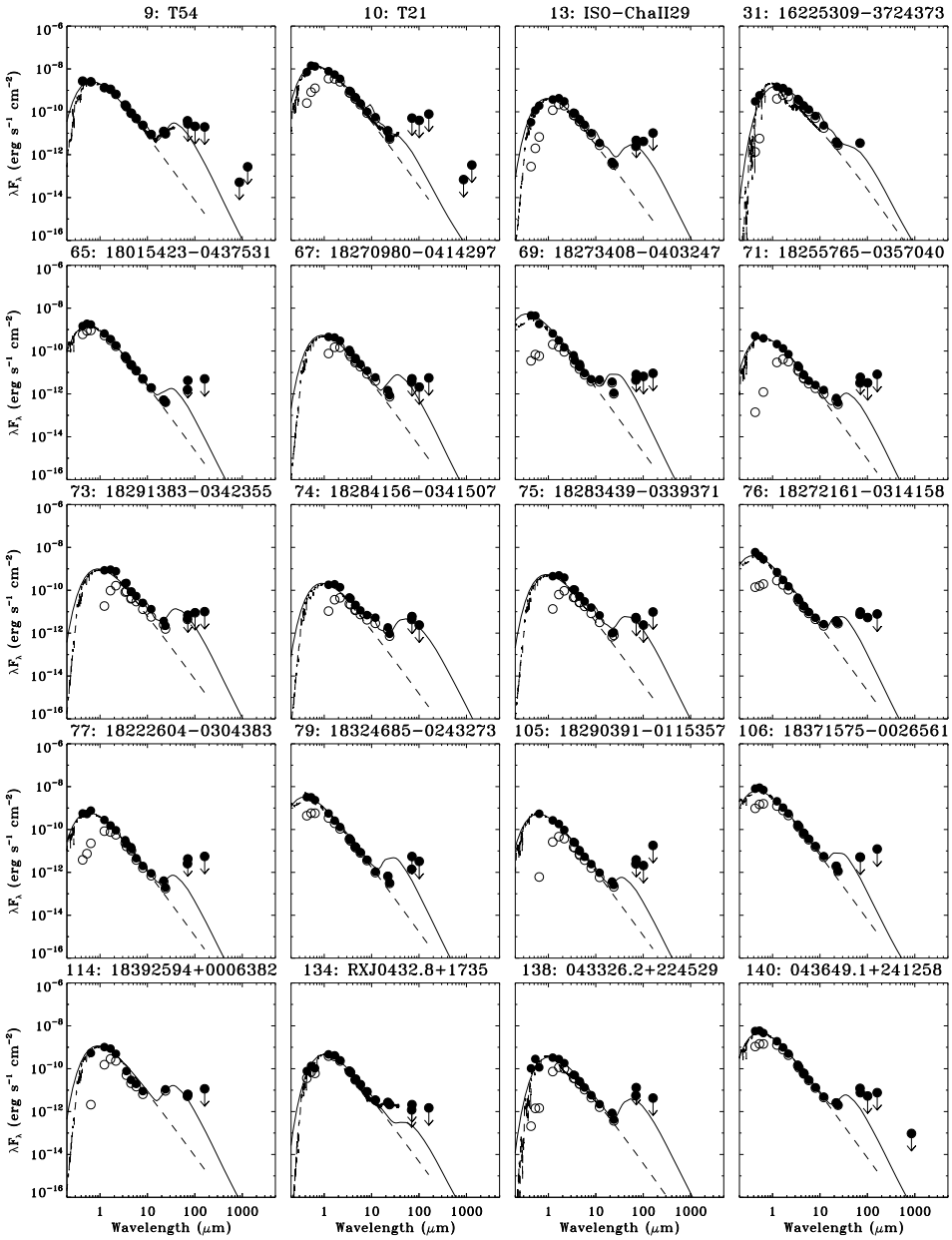

Figure 9.17: *SEDs of low scale height disks.*

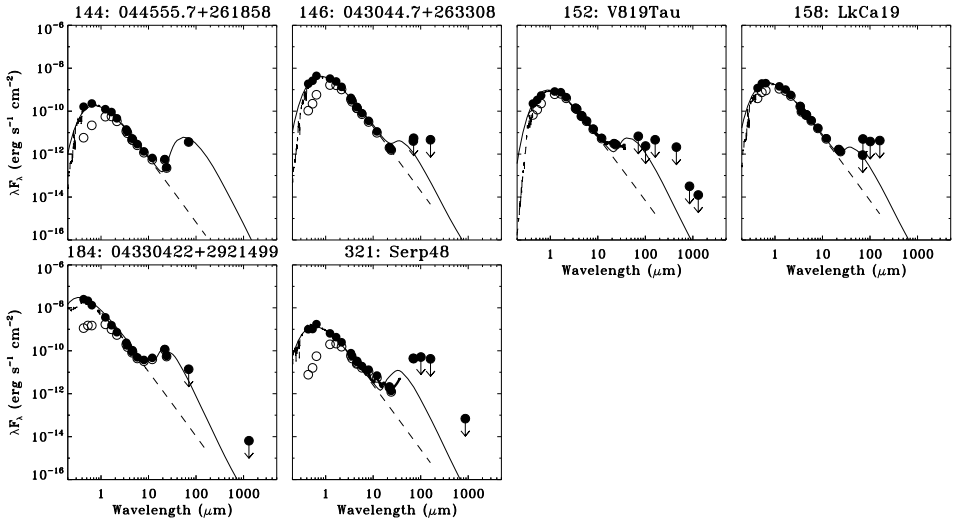

Figure 9.17: *SEDs of low scale height disks.*

9.B Flux tables

This section presents the flux tables.

Table 9.13: *Herschel photometry*

ID	PACS 70 (mJy)	PACS 100 (mJy)	PACS 160 (mJy)	ID	PACS 70 (mJy)	PACS 100 (mJy)	PACS 160 (mJy)
1	4.98±0.5	3.74±0.37	3.17±0.32	65	<0.10	-	<0.27
2	0.22±0.03	0.20±0.04	<0.27	66	0.32±0.05	0.34±0.04	<0.70[a]
3	0.11±0.03	0.14±0.03	<0.26	67	<0.12	<0.07	<0.30
4	<0.10	<0.07[a]	<0.41[a]	68	<0.13	<0.08	<0.34
5	0.18±0.05	0.17±0.03	<0.33[a]	69	<0.19	<0.22	<0.49
6	3.11±0.31	2.90±0.29	2.15±0.25	70	0.63±0.07	0.60±0.06	<0.42
7	0.21±0.04	0.21±0.03	<0.31	71	<0.14	<0.11	<0.44
9	<0.65[a]	<0.71[a]	<1.06[a]	73	<0.16	<0.30	<0.54[a]
10	<1.20[a]	<1.34[a]	<4.21[a]	74	<0.14	<0.08	<-0.02[a]
11	3.86±0.39	3.80±0.38	3.65±0.37	75	<0.11	<0.08	<0.52
12	0.44±0.05	0.40±0.05	<0.39	76	0.23±0.04	0.18±0.04	<0.42
13	<0.11	0.14±0.03	<0.55[a]	77	<0.10	-	<0.30[a]
14	0.69±0.08	0.55±0.06	0.41±0.07	78	<0.14	<0.10	<0.88
15	1.58±0.16	2.31±0.23	2.80±0.28	79	<0.13	<0.11	<-0.08[a]
16	26.06±2.92	36.06±3.9	38.45±6.0	80	<0.18	<0.24	<0.59
17	0.21±0.05	0.25±0.03	0.30±0.09	81	0.44±0.06	0.52±0.06	<0.64
18	0.56±0.07	-	0.45±0.1	82	<0.33[a]	<0.10[a]	<2.61[a]
21	117.78±11.78	100.65±10.06	67.82±6.78	83	<0.12	<0.09	<0.64
23	1.38±0.14	-	1.82±0.2	84	<0.12	<0.07	<0.42
24	0.17±0.04	0.11±0.03	<0.09[a]	85	<0.27	<0.53	<0.05[a]
25	<0.34	<0.32	<0.38[a]	86	<1.05[a]	<1.40[a]	<1.55[a]
26	<0.26	<0.12[a]	<0.02[a]	88	<32.9[a]	<26.25[a]	<59.51[a]
27	0.61±0.07	0.80±0.08	0.96±0.17	89	0.66±0.09	<0.74[a]	<0.59[a]
28	<0.11	<0.15	<-0.11[a]	90	<0.22	<0.22	<1.98
32	0.73±0.08	<1.61[a]	<2.98[a]	91	<0.16	<0.16	<1.05
33	29.8±2.98	28.3±2.83	21.13±2.11	92	<0.31[a]	<0.47[a]	<2.55[a]
34	<2.09	<0.12	<0.06[a]	93	<8.45[a]	<5.27[a]	<10.49[a]
36	<1.44	<1.09[a]	<3.36[a]	94	<0.74[a]	<0.26[a]	<4.44[a]
40	1.89±0.2	1.18±0.15	<3.65	95	<2.27[a]	<2.78[a]	<9.57[a]
41	<0.05[a]	<0.33[a]	<2.70[a]	96	<1.00[a]	<4.13[a]	<-4.57[a]
43	0.38±0.05	0.26±0.05	<0.44[a]	97	<2.49[a]	<6.83[a]	<8.58[a]
44	0.54±0.06	0.74±0.09	<2.02[a]	98	<1.46[a]	<3.07[a]	<10.72[a]
45	10.58±1.06	9.74±0.98	8.96±0.96	99	3.13±0.33	<3.84[a]	<4.62[a]
46	1.14±0.12	1.35±0.14	1.43±0.27	100	0.56±0.07	0.55±0.06	0.56±0.16
47	1.00±0.22	1.15±0.37	<0.49[a]	101	<0.13	0.20±0.05	<27.08
48	0.86±0.09	1.16±0.12	<1.41	102	0.13±0.04	0.31±0.04	<1.05
49	0.26±0.04	<0.14	<0.57[a]	103	0.27±0.06	0.28±0.08	<6.29
50	0.23±0.05	-	<-0.06[a]	104	<0.14	<0.07	<0.22
51	41.14±4.12	27.3±2.77	14.53±4.18	105	<0.09	<0.07	<0.97
52	4.10±0.41	3.66±0.37	2.60±0.5	106	<0.12	-	<0.66
53	<0.14	<0.12[a]	<0.25[a]	107	<0.17	<0.12	<0.75
54	31.58±3.16	25.75±2.58	15.61±1.88	108	<0.14	-	<0.41[a]
55	2.26±0.23	2.15±0.22	2.06±0.35	110	<0.14	-	<0.54
56	1.26±0.39	<2.78	<6.05[a]	111	0.28±0.06	-	<1.93[a]
58	0.34±0.05	<0.28	<0.59[a]	112	<0.11	-	<0.64
59	<0.07	<0.13	<-0.06[a]	113	<0.13	-	<0.38
60	<0.21[a]	<0.32	<0.73[a]	114	0.15±0.04	-	<0.62
61	0.12±0.04	<0.08	<0.56	115	0.40±0.06	0.29±0.08	<0.84
62	1.32±0.14	-	1.62±0.31	116	<0.22	-	<1.02
63	0.97±0.11	0.90±0.1	1.06±0.26	117	<0.13	-	<0.64
64	-	3.48±0.35	3.88±0.84	118	<0.11	-	<0.76

Notes. [(a)] Upper limit due to cloud confusion.

Table 9.13: *Herschel photometry*

ID	PACS 70 (mJy)	PACS 100 (mJy)	PACS 160 (mJy)	ID	PACS 70 (mJy)	PACS 100 (mJy)	PACS 160 (mJy)
119	<0.13	-	<0.02[a]	179	1.23±0.13	1.41±0.14	1.69±0.19
120	<0.13	<0.08	<2.04	180	0.30±0.04	0.24±0.03	<0.25
121	<0.59[a]	-	<0.45[a]	181	<0.44[a]	<0.33[a]	<0.92[a]
122	<0.10	-	<0.07[a]	182	<-0.07[a]	<-0.03[a]	<-0.72[a]
123	0.13±0.04	<0.07	<0.38	183	<0.48	<0.39[a]	<1.73[a]
124	<0.11	<0.07	<0.55	185	0.21±0.06	0.24±0.05	<0.91
125	1.42±0.15	-	<1.14	187	2.41±0.24	2.60±0.26	2.02±0.22
126	<16.95	<33.54	<3.04[a]	188	0.48±0.1	0.33±0.11	0.32±0.08
127	0.34±0.05	0.18±0.03	<8.11	189	0.75±0.09	0.91±0.09	1.25±0.16
128	<0.12	<0.10	<1.26	190	<0.15	-	<0.59
129	<0.12	-	<0.10[a]	191	0.35±0.07	0.27±0.04	0.37±0.11
130	<0.15	-	<0.55	192	0.52±0.09	-	0.48±0.16
131	<0.12	0.16±0.03	<0.46	193	0.33±0.05	0.35±0.04	<0.57
132	3.03±0.31	2.64±0.27	2.41±0.28	194	0.43±0.06	0.41±0.05	0.63±0.18
133	0.44±0.06	0.46±0.07	<0.94	195	0.29±0.06	-	<0.30
134	<0.05	-	<0.08	196	1.60±0.17	1.16±0.12	0.77±0.1
135	0.77±0.08	0.84±0.09	0.85±0.17	197	0.60±0.08	-	0.64±0.15
136	3.21±0.32	-	2.68±0.28	198	1.35±0.15	-	0.92±0.14
137	0.29±0.04	-	0.42±0.09	200	0.48±0.06	0.37±0.05	0.47±0.15
138	<0.31	-	<0.23[a]	201	0.22±0.05	0.21±0.03	<0.26
139	0.46±0.07	-	<0.37	202	1.73±0.3	<1.95	<1.53[a]
140	0.18±0.05	<0.18[a]	<0.41	203	2.39±0.25	-	3.30±0.38
142	20.39±2.04	17.59±1.76	12.65±2.57	204	<73.51	<60.36	<9.49[a]
145	0.44±0.06	0.45±0.05	0.35±0.09	301	0.26±0.05	0.24±0.05	<0.73
146	<0.13	-	<0.25	303	1.63±0.17	2.88±0.29	3.90±0.4
147	0.17±0.06	-	<0.50	307	3.63±0.37	-	3.24±0.33
148	0.48±0.08	-	<0.43	309	<3.93[a]	-	<7.50[a]
149	53.78±5.39	39.92±4.05	22.87±3.33	310	0.62±0.07	-	1.55±0.18
150	0.49±0.07	0.42±0.08	<3.51	314	0.68±0.07	0.61±0.08	0.81±0.26
151	0.26±0.05	-	0.47±0.12	317	1.08±0.11	0.69±0.07	<0.38
152	<0.16	<0.08	<0.25	318	<21.71[a]	<17.06[a]	<16.7[a]
153	13.82±1.38	-	8.36±0.86	319	0.89±0.1	0.70±0.12	<1.82[a]
154	0.66±0.09	0.64±0.07	0.44±0.11	321	1.02±0.11	<1.72[a]	<2.26[a]
155	1.26±0.14	1.34±0.14	1.11±0.13	322	0.51±0.07	0.47±0.05	0.70±0.14
156	<0.15	-	<0.36	325	1.20±0.13	1.45±0.15	1.77±0.38
157	0.21±0.05	<0.10	<0.37	326	1.03±0.11	0.92±0.09	1.36±0.35
158	<0.12	<0.13	<0.23	329	2.93±0.3	-	4.34±0.44
159	131.87±13.19	-	67.75±6.79	334	<0.10	-	0.28±0.09
160	0.30±0.05	0.20±0.03	<0.64	335	0.49±0.15	<0.99	<2.39
161	<23.85	<23.35	<0.67[a]	336	<0.12	0.13±0.02	<0.18
162	0.38±0.08	0.44±0.09	<2.46				
163	<14.92	<26.05	<5.67[a]				
164	<0.13	<0.14	<0.85				
165	<0.14	<0.18	<1.01				
166	3.20±0.32	3.15±0.32	2.28±0.43				
167	0.17±0.05	0.25±0.05	<1.64				
168	<0.12	<0.09	<1.14				
169	<0.39	<0.80	<0.43[a]				
171	0.40±0.06	0.34±0.07	<2.01				
172	0.37±0.06	0.32±0.05	<0.77				
173	11.41±1.14	10.25±1.03	7.38±0.74				
174	<0.58[a]	<1.03[a]	<3.80[a]				
175	1.35±0.14	1.58±0.16	1.87±0.27				
176	<0.11	<0.06	<0.25				
177	<0.11	<0.06	<0.46				
178	2.47±0.36	4.41±0.76	10.19±1.65				

Table 9.14: *Submillimeter photometry*

ID	SABOCA [350 μm] (mJy)	LABOCA [870 μm] (mJy)	SCUBA [450 μm] (mJy)	SCUBA [850 μm] (mJy)	SMA [880 μm] (mJy)	230 GHz [1.3mm] (mJy)	110 GHz [3.3mm] (mJy)	Ref
1	2400±200	210±20				105±150	7±1	1,2
2		<40						1
6	690±180	197±12.2					8.8±1.5	1,3
9		<15				<118		1,2
10		<20				<143		1,2
11	2400±500	314±12				77.5±20.3	2.3±0.4	1,4
12						<100		2
14		24±6				47.8±15.5		1,2
15	4000±200	420±50				124.9±24	6.2±1.5	1,2
16	9800±2400	1500±10					33.1±1.2	1,3
18		20±6				<105		1,2
20	1000±200	390±10				224±8	22±3.3	1,5
21					2700±270	1190±30	47±6	6,7
22	<300			<31.4				1
23				153.2±11.5		49±4.8	5.7±0.7	1,4
24		<23.2				<13		8,4
25		<30				<57		1,9
26				<30.5		<42		1,9
27	190±40	35±3				<27		1,4
28		<21						8
29				30.8±6.6		<11.4		1,10
32	<82			<36.8				1
33			4200±840		620±62			11,12
35		<30				<45		1,4
36	<220			72.6±18.5				1
38			919±184		430±43	132±3.9	6.7±0.6	13,12
39	3154±419		2042±111	770±39		451±20		14
40	<700	<20				<8.4		1,10
41						<9.6		10
43		<18						1
44				37.8±11		9.3±3		1,10
45			1900±380		550±55			13,12
46	800±200	164±14				81.8±2.7		1,10
47				<50.1				1
49				<13				10
50						<5.4		15
51			950±200	180±18		60±6		16,17
52					210±21			12
54			3300±660		400±40			13,12
55	<900	92±6						1
56				<59.1				1
58		<18						1
60				<24.2		<11.4		1,10
62	<600	62±9				24.5±3.1		1,10
63				95.2±16.4				1
64					238±24	67.5±1.4		18
70				32.4±10.7				1
82				<57.1				1

Refs. 1) This work. 2) Henning et al. (1993), 3) Lommen et al. (2007), 4) Lommen et al. (2010), 5) Gräfe & Wolf (2013), 6) Fukagawa et al. (2013), 7) Verhoeff et al. (2011), 8) Romero et al. (2012), 9) Merín et al. (2008), 10) Cieza et al. (2010), 11) Pérez et al. (2014), 12) Andrews et al. (2011), 13) van der Marel et al. (2015c), 14) Jensen et al. (1996), 15) Merín et al. (2010), 16) van der Marel et al. (2013), 17) Brown et al. (2012a), 18) Mathews et al. (2012), 19) Andrews et al. (2013), 20) Cieza et al. (2012b), 21) Andrews & Williams (2007b), 22) Andrews & Williams (2005), 23) Enoch et al. (2006), 24) Nuernberger et al. (1997), 25) Isella et al. (2009), 26) Hughes et al. (2010)

Table 9.14: *Submillimeter photometry*

ID	SABOCA [350 μm] (mJy)	LABOCA [870 μm] (mJy)	SCUBA [450 μm] (mJy)	SCUBA [850 μm] (mJy)	SMA [880 μm] (mJy)	230 GHz [1.3mm] (mJy)	110 GHz [3.3mm] (mJy)	Ref
86				<107.1				1
88				<137.3				1
89				<35.4				1
92				<79.3				1
95		49±11						1
98		63±8						1
99		360±30						1
100				<36.8				1
107				<17.3				1
113				<18.2				1
115						<22.8	<1.9	4,4
120				<21.1				1
124				<19.2		24±0.6		1,15
127				<29.2		6.3±0.6		1,15
131						2.3±0.6		15
132		109±11						1
135					210±21			12
136					150±15			12
137				63.2±18		31±2		1,19
140				<27				20
142					180±18			12
145					49±4.9			21
148			<516	34±5		16±5		22
149			2570±350	638±54		234±19		22
150						<3.3		20
152			<317	<9		<5.4		22
153			1920±160	560±30		229±17		22
154				<55.8		15±1		1,19
155				54.5±17.7				1
156				<31.4				1
159			3820±570	359±67		103±18		22
161				<115.1		3.7±0.9		1,15
162						6.3±1.1		15
163				<117.4				1
165						<1.4		15
166				166.7±14		126±12		1,23
168						<1.4		15
171				17.3±5.7				1
172				31±6				20
173					210±21			12
174				<26.9		9.7±1.5		1,20
175					10±2			20
177						<2.5		20
178				222.4±16.3				1
179		100±5						8
180		<21						8
181						<1.1		20
182						<3		20
183						<1.5		20
184						<2.8		20
185						<27		9
187	680±114			125.5±18.3		41±5		22,1
188			<442	32±8		<36		22
189				93.4±15.7				1

Table 9.14: *Submillimeter photometry*

ID	SABOCA [350 μm] (mJy)	LABOCA [870 μm] (mJy)	SCUBA [450 μm] (mJy)	SCUBA [850 μm] (mJy)	SMA [880 μm] (mJy)	230 GHz [1.3mm] (mJy)	110 GHz [3.3mm] (mJy)	Ref
190						8.4±1.4		19
192				<28.6				1
193				31.9±9.4				1
194						13.4±1.4		19
196				69.3±18.8				1
197			<456	130±7		47±0.7		22
198			<291	90±7		36±5		22
200		<40				26±9		1,24
202				<55.5				1
203		55±10						1
303		136±7						1
307		123±14						1
316		98±13						1
321		<20						1
325			1310±260		410±41			13,12
329					640±64	189±15		12,25
333				<56.1				1
349						49±9		26
350						60±8		26

Acknowledgements. The authors would like to thank C. Manara for useful discussions and M. McClure for providing the IRS spectrum on DoAr28. N.M. is supported by the Netherlands Research School for Astronomy (NOVA). Astrochemistry in Leiden is supported by the Netherlands Research School for Astronomy (NOVA), by a Royal Netherlands Academy of Arts and Sciences (KNAW) professor prize, and by the European Union A-ERC grant 291141 CHEMPLAN. This publication makes use of data products from the Wide-field Infrared Survey Explorer, which is a joint project of the University of California, Los Angeles, and the Jet Propulsion Laboratory/California Institute of Technology, funded by the National Aeronautics and Space Administration. The William Herschel Telescope is operated on the island of La Palma by the Isaac Newton Group in the Spanish Observatorio del Roque de los Muchachos of the Instituto de Astrofísica de Canarias.